Engineering Structures 322 (2025) 119043

Contents lists available at ScienceDirect

Engineering Structures

journal homepage: www.elsevier.com/locate/engstruct

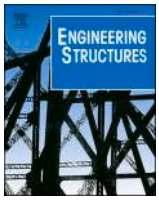

RC dapped-end beams with various reinforcement layouts: An experimental investigation

Giovanni Menichini, Federico Gusella, Salvatore Giacomo Morano, Maurizio Orlando *

University of Florence, Department of Civil and Environmental Engineering, Italy

ARTICLE INFO

Keywords:
RC discontinuity regions
Experimental tests
Half-joints
Dapped ends
Crack pattern

ABSTRACT

Reinforced Concrete (RC) discontinuity regions (D-regions), such as dapped ends, can represent vulnerable zones in existing RC structures since they can exhibit a brittle failure mechanism. In common design practice, the ultimate strength of D-regions is assessed through Strut and Tie (S&T) models. Current design codes recommend two resistant mechanisms for dapped ends but do not provide information about the identification of steel bars involved in the resistant mechanism when the reinforcement is formed by distributed bars. An experimental campaign on dapped-end beams with various reinforcement layouts, including configurations without diagonal bars or with one or multiple layers of diagonal bars, has been carried out at the Structures and Material Testing Laboratory of the Department of Civil and Environmental Engineering in Florence. Results allow for identifying the influence of different reinforcement layouts on the crack pattern at the Service Limit State (SLS) and on the post-peak response. Both the strain on bars and the crack opening displacements are investigated until failure. The work highlights that layouts with distributed diagonal bars reduce the crack widths at the SLS compared to other configurations, increase the ductility, and allow for the timely detection of damaged dapped ends during in situ inspections.

1. Introduction

Dapped ends (or half-joints) sustain suspended spans of reinforced concrete (RC) bridges (Fig. 1) and determine an isostatic scheme, avoiding the stress increase in case of foundation settlements or thermal deformations. Half-joints represent critical zones, often affected by a brittle failure, as observed in recent collapses [1,2]. Stress distribution is influenced by the reinforcement layout, whose effect has been experimentally investigated in [3–11]. It has been highlighted that three failure modes mainly affect the collapse of dapped ends: the nib failure, with a crack extending from the inner corner of the nib at an angle inclined to the longitudinal axis of the beam, the flexural failure of the beam full-depth section, and a failure mode with cracks developing from the bottom corner of the full-depth section [12,13]. Experimental tests highlighted the significant impact on the resistance due to a proper anchorage of the longitudinal reinforcing bars in the nib and the need to provide enough hanger reinforcement. The importance of structural details was underlined in [5,14], where specimens with an accurately detailed reinforcement, such as the anchorage of the longitudinal reinforcement at both the top and bottom of the beam, developed a higher strength.

The beneficial effect of diagonal bars under service loads, because of the reduction of the crack widths, was underlined in [12,13]; moreover, specimens equipped with diagonal bars showed a higher ultimate resistance [5,15].

In [16] it was observed that the crack pattern reduces as the first vertical hanger reinforcement approaches the nib and the strength increases with the reduction of the length-to-depth ratio of the nib. In [17,18] it was highlighted that higher-strength concrete and low flexural tensile reinforcement ratios ensure sufficient ductility.

The resistance of half-joints is usually estimated by S&T models [14,19,20]. In [21] a method based on the kinematics, equilibrium and constitutive relationships, whose accuracy was confirmed through the investigation of a database of 47 tests, has been proposed. Nevertheless, the method requires direct use of on-site measurable data and then appears difficult to apply in common practice. Within the work [22] the authors developed a mechanism analysis method, based on the upper-bound theorem of concrete plasticity, to predict the critical failure

* Corresponding author.
E-mail addresses: giovanni.menichini@unifi.it (G. Menichini), federico.gusella@unifi.it (F. Gusella), salvatoregiacomo.morano@unifi.it (S.G. Morano), maurizio.orlando@unifi.it (M. Orlando).

https://doi.org/10.1016/j.engstruct.2024.119043
Received 17 May 2024; Received in revised form 6 August 2024; Accepted 23 September 2024
Available online 5 October 2024

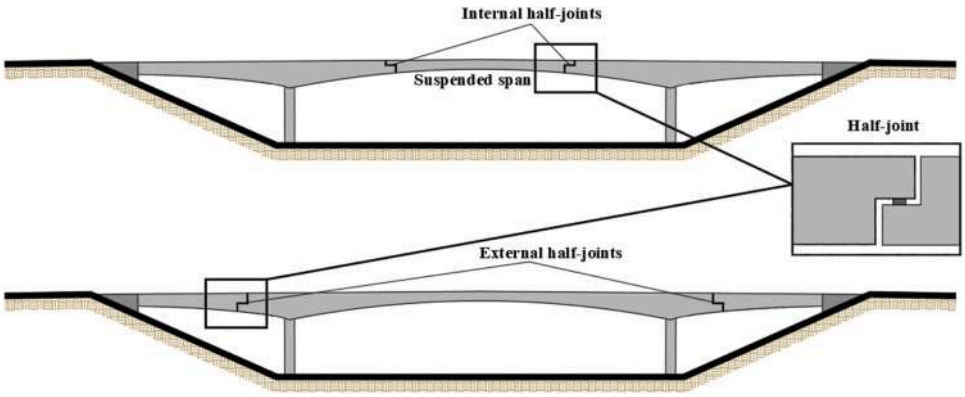

Fig. 1. Identification of half-joints.

plane and the shear capacity of reinforced concrete dapped-end beams. In [23] a model, capable of estimating the effective numbers of vertical rebars involved in the resistant mechanism, has been developed. The application of S&T models remains the method capable of better predicting the resistance of D-regions [24,25], nevertheless, conventional S&T models, such as those given in the Eurocode 2 [26], are drawn for half-joints with concentrated ties and require adjustments to be used for predicting the load-carrying capacity of half-joints with distributed reinforcement. Specific guidelines [27–30] have been developed for the assessment of existing reinforced concrete dapped ends, through monitoring and investigation strategies considering the corrosion of rebars [31,32], but do not provide an accurate method for estimating their expected ultimate load capacity.

The effective resistance of half-joints can be well predicted by Finite Element (FE) models, which showed satisfactory results even if limited to previous experimentally investigated joints. In [4,33,34] numerical models were developed to estimate the effect of strengthening works; examples can be found in [8,19,35–37]. The drawbacks of FE models remain the time-consuming and the lack of information on both mechanical properties and structural details, which usually characterize existing structures in common practice.

In summary, literature studies indicate that the impact of reinforcement layouts can be significant, requiring potential adjustments to common literature S&T models for correctly estimating the resistant capacity of specific existing half-joints. Finally, experimental tests are the most reliable tool for evaluating the actual capacity of half-joints. Experimental data can then be utilized to refine the geometry of S&T models, enabling accurate evaluation of the strength capacity also in the presence of distributed reinforcement [11,38,39].

1.1. Aim of the work

Results of an experimental campaign, performed at the Structures and Material Testing Laboratory of the Department of Civil and Environmental Engineering of the University of Florence, are presented. Investigated specimens are characterized by three different reinforcement layouts. The tests are primarily aimed at identifying the influence of reinforcement layout on the crack pattern, the distribution of forces in steel rebars, and the post-peak response.

The paper is organized as follows. Firstly, the geometrical characteristics and structural details of specimens are described. Then the test setup, loading protocol and the mechanical properties of the materials are presented. In the subsequent section, results are discussed highlighting how the load-carrying capacity of dapped ends is impacted by different reinforcement layouts. The paper proceeds to highlight the crack pattern until the failure and the influence of the reinforcement layout on the post-peak structural response.

2. Experimental campaign

2.1. Investigated specimens

Three types (T1, T2 and T3) of full-scale RC dapped ends are tested. The geometry and reinforcement layout are shown in Fig. 2 and identified in Table 1.

Two beams for each dapped-end type have been cast for a total of six dapped-end beams; then, each dapped end has been labeled as follows: Tα-βΔ, where: $\alpha = 1, 2, 3$ denotes the dapped end; $\beta = 1, 2$ denotes the absence (1) or presence (2) of strain gauges in some bars; $\Delta = A, B$ distinguishes the two dapped ends of the same beam (left side or right side).

A total of nine dapped ends are tested (Table 1). Type T1 includes three specimens: in two of them (T1–1A and T1–2B) the bottom longitudinal bars are provided with an anchorage steel plate, while in the third specimen (T1–2A*) the anchorage plate is missing to evaluate its influence on the structural response and failure mode. Type T2 includes two specimens (T2–1A and T2–2A), while type T3 includes four specimens (T3–1A, T3–1B, T3–2A, T3–2B).

All specimens were constructed using concrete of grade C25/30 (f_{ck}=25 N/mm^2) and steel rebars of grade B450C (f_{yk}=450 N/mm^2).

For each beam of the types T1 and T2, tests were performed on one dapped end, while the other dapped end of the same beam was tested after strengthening it with a post-installed threaded bar. The results of reinforced dapped ends will be presented in a companion paper. In beams of type T3, tests were performed on both dapped ends of each beam, as the high reinforcement density has made it impracticable to install the reinforcing threaded bar.

Besides the vertical stirrups at 75 mm intervals, in specimens of type T1 there are two 16 mm horizontal U bars; in specimens of type T2 there are two 8 mm horizontal U bars and a couple of 12 mm diagonal bars (Fig. 2), whose top ends are intentionally not vertically aligned with the support of the nib, as is common practice; and in specimens of type T3, there are four couples of diagonal bars (n.4 ×2Φ8) at 50 mm intervals (Fig. 2). In all specimens there are two vertical Φ14 bars and the first stirrup is always positioned 120 mm from them to account for the potential presence of a cross beam (dashed area in Fig. 2). The three chosen layouts resemble those of existing Italian bridges [2,32,38,40,41] (Fig. 3).

2.2. Reinforcement dimensioning of specimens using Strut & Tie models and a preliminary FE model

The reinforcement dimensioning of specimens was performed using S&T models and a FE model. S&T models for dapped ends are shown in Fig. 4. The first model (*Truss 1*) is taken from EC2, but with the anchorage of the horizontal tie $H_{1,1}$ modified according to Schlaich [44], and can be used for the analysis of dapped ends equipped with vertical

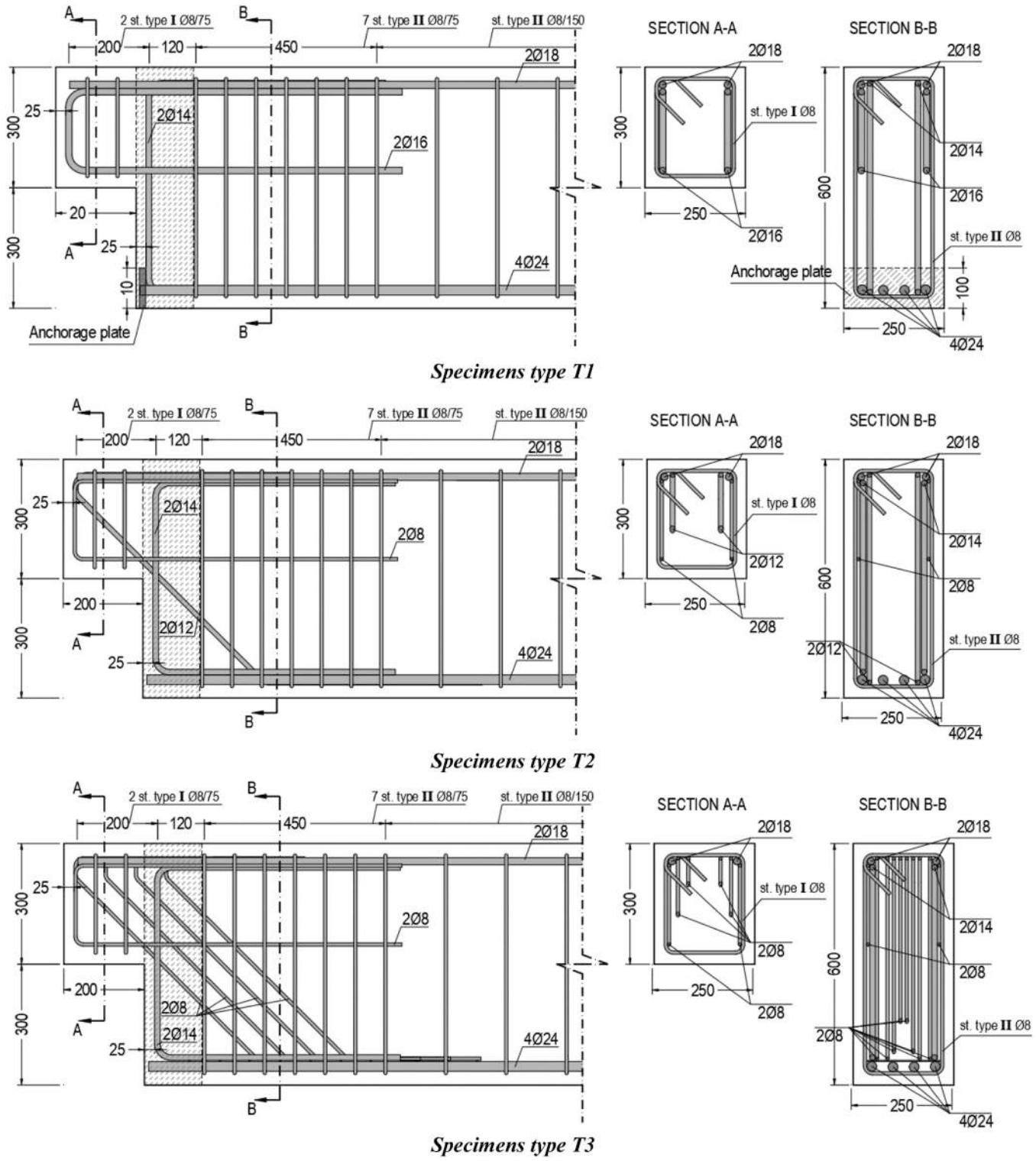

Fig. 2. Geometry and reinforcement layout of the three dapped end types.

and horizontal reinforcement. The second model (*Truss 2*), also taken from EC2, is valid in the presence of diagonal reinforcement only.

In Truss 1 (Fig. 4) the vertical reinforcement is represented by one tie ($T_{1,1}$), as is the case of one bar only or more bars positioned in a narrow band. If more vertical bars are distributed over a significant band, like in T1 specimens, preliminarily the position and the cross-section of the equivalent vertical tie $T_{1,1(eq)}$ should be identified. To this aim, an iterative procedure can be used for T1 specimens, where initially Truss 1 includes only the first 14 mm vertical bars. Subsequently, Truss 1 is modified to incorporate the first stirrup along with an additional inclined strut connecting the support and the top end of the second stirrup. The procedure continues with adding other stirrups, one after the other, until the force in the horizontal tie equals its yield strength ([23]), provided the concrete does not crush prematurely. Under the assumption that the yielding of reinforcement precedes the concrete crushing and that the yield stress of steel holds $f_y = 500$ N/mm^2, the iterative

Table 1
Reinforcement of all specimens (unit of length: mm).

Specimen type	Specimen label	Stirrups (two legs)	Diagonal bars	U-reinforcements	N. of tests #
T1	T1 – 1A T1 – 2A* T1 – 2B	Φ14 + Φ8/ 75	//	2Φ16	3
T2	T2 – 1A T2 – 2A	Φ14 + Φ8/ 75	2Φ12	2Φ8	2
T3	T3 – 1A T3 – 1B T3 – 2A T3 – 2B	Φ14 + Φ8/ 75	2Φ8/50	2Φ8	4

* In specimen T1–2A* the bottom longitudinal reinforcement of the beam is not provided with the anchorage steel plate.

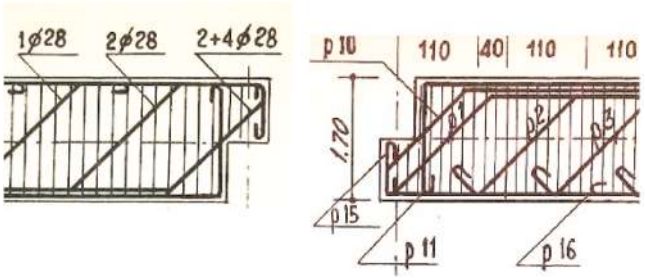

Fig. 3. Examples of reinforcement layouts in dapped-end beams of existing Italian bridges [42].

procedure based on Truss 1 provides an ultimate external load of 373 kN for specimens of type T1.

For specimens of types T2 and T3, the reinforcement layout cannot be directly associated with either Truss 1 or to Truss 2. This is due to the simultaneous presence of vertical and diagonal bars on one side, and distributed bars instead of concentrated bars on the other side. The interaction between Truss 1 and Truss 2 is still an open issue, and their linear combination may not provide a reliable estimate of the ultimate capacity of dapped ends with both vertical and diagonal bars. Based on this consideration, the reinforcement dimensioning for specimens of types T2 and T3 was performed numerically using a nonlinear 2D finite element (FE) model, which was first validated by verifying that it provided a resistance capacity for T1 specimens comparable to that determined with the S&T technique. The FE model (Fig. 5) was developed in DIANA 10.6 [44], using 3831 plane stress elements and a 25 mm mesh size. The total strain rotating crack model with elastic perfectly plastic behavior in compression and zero tensile strength in tension was used. To simulate longitudinal and transverse reinforcement, embedded truss elements with perfect bond to concrete and a perfectly plastic behavior were adopted. A vertical-axis roller was introduced under the nib and under the beam, and a horizontal-axis roller was applied to the midpoint of the load plate, to achieve an isostatic configuration. A mechanical non-linear analysis under displacement control was performed until failure, imposing a vertical displacement to the top of the load plate.

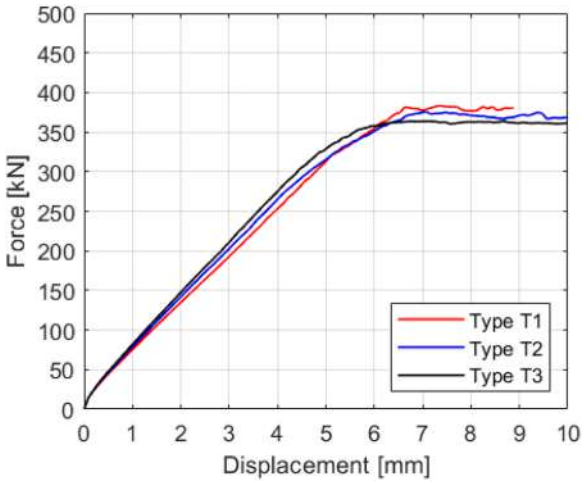

Fig. 6. Specimen capacity curves estimated through FE numerical model.

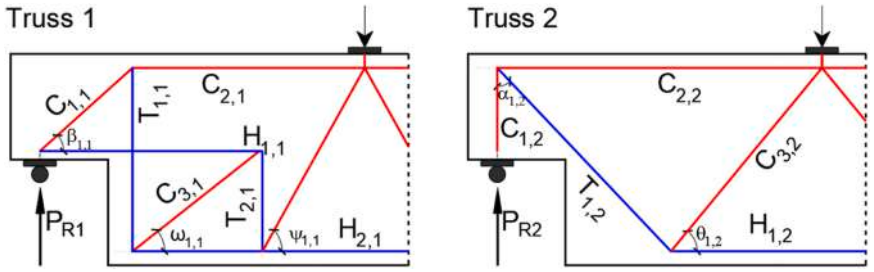

Fig. 4. a) S&T model suggested by EC2 for horizontal and vertical bars and modified according to Schlaich et al. [43] b) S&T model suggested by EC2 for diagonal bars (ties in blue –struts in red).

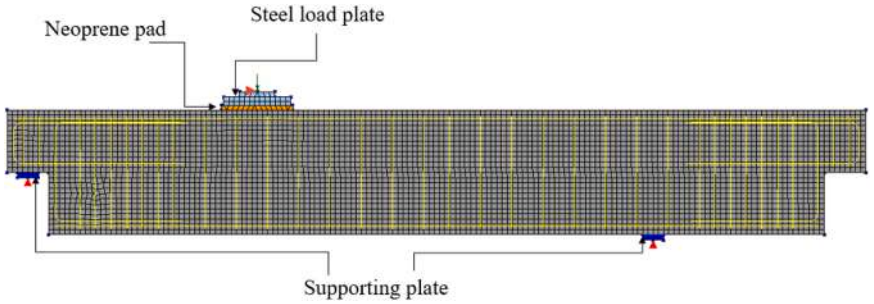

Fig. 5. DIANA FEA numerical model.

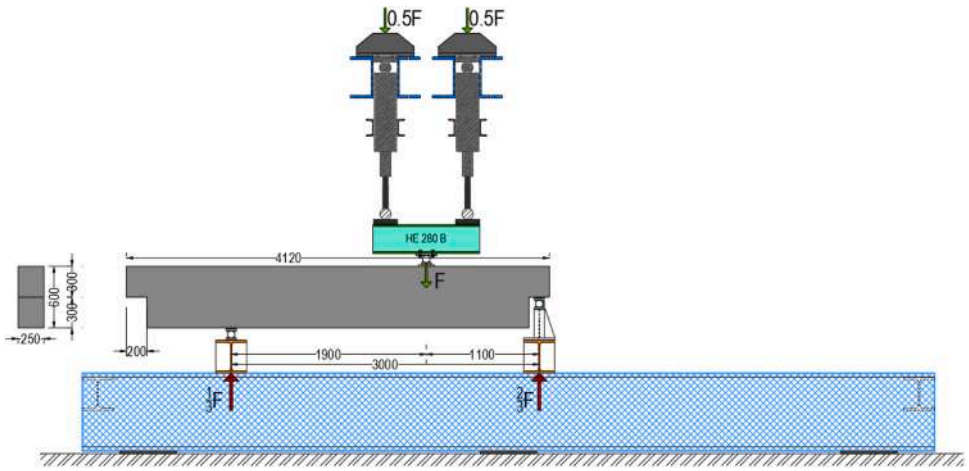

Fig. 7. Three-point non-symmetric bending test with identification of the reactions at external supports [mm].

The following average values of the compression strength and secant elastic modulus of concrete were assumed: $f_{cm}=f_{ck}+8=33$ N/mm^2, $E_{cm}=22\ (f_{cm}/10)^{0.3} \cong 31{,}500$ N/mm^2. The concrete tensile strength was neglected. For the steel rebars, an average yield strength of 500 N/mm^2 and an elastic modulus of 200000 N/mm^2 were adopted.

The numerical external ultimate load evaluated through the FE model for T1 specimens holds 383 kN, which is only slightly higher than the analytical value of 373 kN calculated with the modified Truss 1 model. The FE model was then used to determine the reinforcement amounts for specimens of types T2 and T3 (Fig. 2) to achieve about the same ultimate load of T1 specimens. Adopting the bar diameters described above, the following values were obtained: 377 kN and 366 kN for T2 and T3 specimens, respectively. The numerical curves of external load versus displacement at loaded point *f*or all three specimen types are shown in Fig. 6.

The finite element analyses were employed solely for the dimensioning of the reinforcement and not for replicating the experimental results. Therefore, they were not utilized for identifying the cracking pattern and in general the damaged zones of the specimens, which was beyond the aim of the paper. In the continuation of research, additional FE models to simulate experimental results are being developed utilizing more refined constitutive laws for concrete in compression and considering also its tensile strength. To this aim the average experimental values of the mechanical parameters will be used, which were not available at the time of designing the specimens.

2.3. Geometry of specimens and test setup

The overall length of each dapped-end beam is 4120 mm, with a rectangular full-depth cross-section of 250 × 600 mm^2 (Fig. 7). The length of the nib is 200 mm, while its depth is set equal to 300 mm (half of the full depth of the beam). All beams are cast adopting the same longitudinal and transversal reinforcement layout of the full-depth section, with a minimum effective concrete cover of 25 mm. Top and bottom flexural reinforcements are oversized and provided along the full length of the beam, to prevent flexural failure. Shear reinforcement comprises Φ8 vertical stirrups placed at variable spacings (from 75 mm to 150 mm, near and far from the dapped ends, respectively) and it is designed to prevent the shear failure of the beam.

All beams are subjected to three-point non-symmetric bending, under simply supported conditions (total span equal to 3000 mm, Fig. 7). The vertical load is applied at 1100 mm (about one-third of the beam span length) from the support of the tested dapped end using two electromechanical actuators with a maximum load capacity of 350 kN each. The distance (1100 mm) between the point of application of the external load and the vertical support under the nib is equal to two times the effective depth of the beam (550 mm) to avoid the formation of a direct strut between the load plate and the support, as recommended in [11,12,26,31].

The load F is transferred to the specimen through a rigid steel beam HE 280 B (Fig. 7). Both supports, whether beneath the beam end or the tested dapped end, are composed of a welded 50 mm diameter steel cylinder. The reactions at the supports (F/3 beneath the beam end and 2 F/3 beneath the dapped end) are shown in Fig. 7. A Teflon pad is placed between the loading device and the top surface to uniformly distribute the load, preventing stress concentrations. The same is done between the bottom surface and both supports by using 2 mm thick Teflon sheets. The loading device and the structural setup are shown in Fig. 8.

2.4. Mechanical properties

2.4.1. Concrete

The concrete composition mirrors the typical practices of concrete production in Italy during the 1980s: 325 kg/m^3 of cement type CEM 42.5 II/A-LL, a free water/cement ratio of 0.70, 300 kg/ m^3 of siliceous fine aggregates (0–2 mm), 540 kg/ m^3 of limestone fine aggregates (0–5 mm), 890 kg/ m^3 of limestone coarse aggregates (5–30 mm) and 1.4 l/ m^3 of fluidizing additive (SNF); the consistency class is S5.

The compressive strength of concrete is estimated through five uniaxial compression tests on cylinder specimens (diameter x length = d x L ≈ 100 mm × 190 mm) according to EN 12390–3 [45]. The age of the specimens, dimensions, weight, cross-section area, maximum load, and strength (f_c) are listed in Table 2. Compression tests provide an average cylinder compressive strength $f_c \approx 40.4$ N/mm^2 with a standard deviation of 3.1 N/mm^2 (Table 2). Note that the first compression tests were executed after about three months from the cast of beams when tests on dapped ends started.

The tensile strength is evaluated through five splitting tensile tests, according to EN 12390–6 [46]. Results are listed in Table 3.

The average splitting tensile strength (f_{ct}) is 4.27 N/mm^2 with a standard deviation of 0.58 N/mm^2, where the tensile strength for each specimen is obtained as $f_{ct} = \frac{2P_{max}}{\pi L d}$, being P_{max} the maximum load, L [mm] the specimen length and d [mm] the diameter of the cylinder. The concrete compressive strength has been also evaluated at a testing age of 320 days through compression tests on twenty-three core specimens drilled from beams after completing tests on dapped ends. Results are listed in Table 4 and allow for estimating an average cylinder compressive strength $f_c \approx 40$ N/mm^2 with a standard deviation of 3 N/mm^2. The average compressive strength of core specimens after more than ten months from casting is nearly identical to that of cast specimens tested after three months from casting (Table 5); the same holds for the

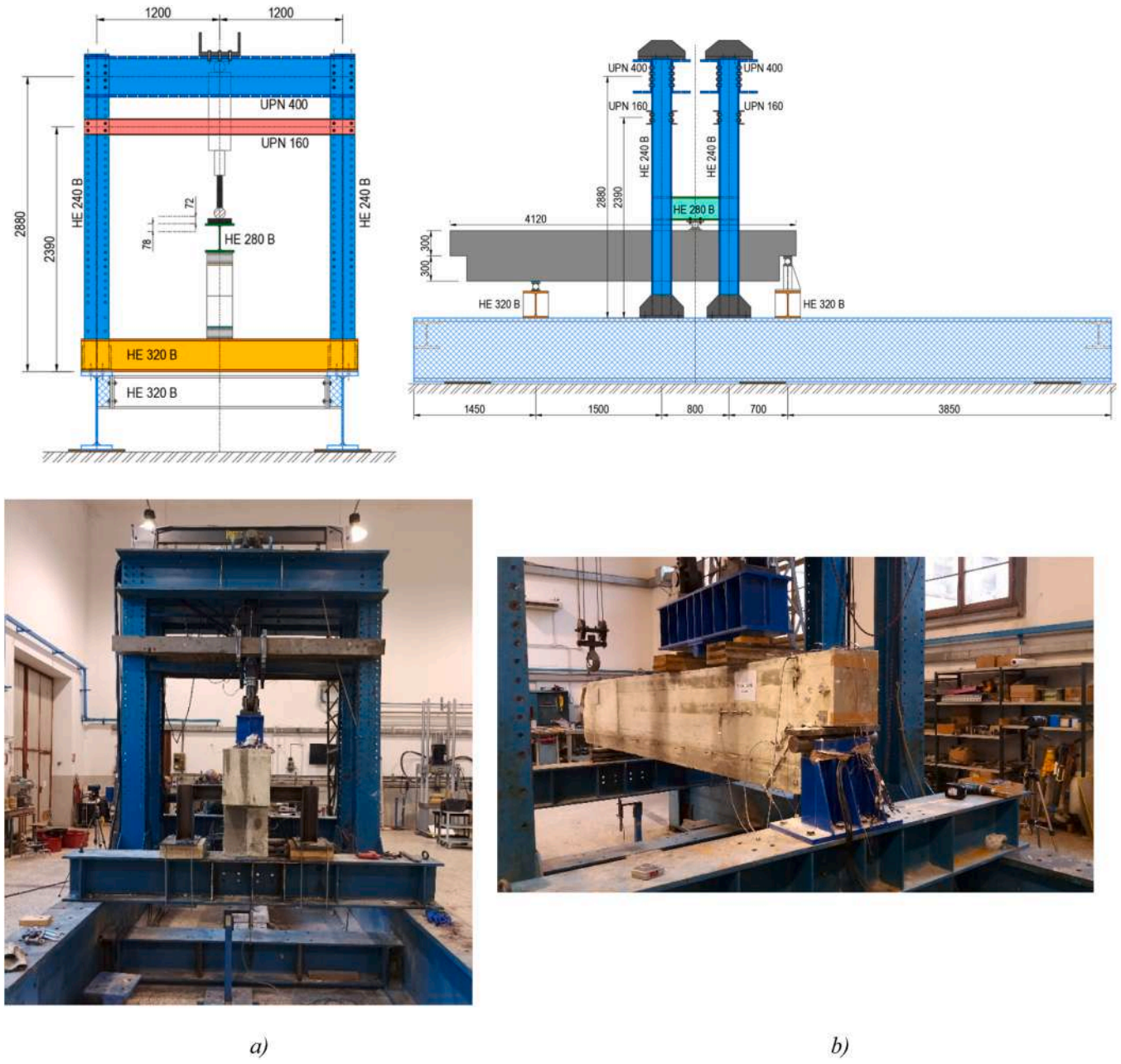

Fig. 8. Test setup. a) Frontal view b) Lateral view.

Table 2
Concrete mechanical properties estimated through compression tests on cylinder specimens.

Test	Age	Dimensions		Weight	Cross-section	Maximum Load	f_c
	[dd]	d [mm]	L [mm]	[g]	[mm^2]	[kN]	[N/mm^2]
1	96	100	192	3437	7854	294	37
2	98	100	191	3446	7854	298	38
3	98	100	191	3452	7854	302	38
4	271	100	193	3153	7823	352	45
5	272	100	192	3484	7823	340	43
Mean (μ) – Std (σ)							$\mu = 40.4$ - $\sigma = 3.1$

Table 3
Concrete mechanical properties estimated through splitting tests on cylinder specimens.

Test	Age	Dimensions		Weight	Cross-section	Maximum Load	f_{ct}
	[dd]	d [mm]	L [mm]	[g]	[mm^2]	[kN]	[N/mm^2]
1	96	100	190	3444	7854	130	4,34
2	96	100	191	3432	7854	98	3,27
3	96	100	191	3427	7854	132	4,38
4	247	100	194	3505	7854	141	4,61
5	247	100	193	3513	7823	143	4,75
Mean (μ) – Std (σ)							$\mu = 4.27$ - $\sigma = 0.58$

Table 4
Concrete compressive strength from compression tests on core specimens.

Test	Age	Dimensions		Weight	Cross-section	Maximum Load	f_c
	[dd]	d [mm]	L [mm]	[g]	[mm^2]	[kN]	[N/mm^2]
1	320	94	191	3004	6940	288	41
2	320	94	195	3027	6940	298	43
3	320	94	190	2974	6940	287	41
4	320	94	191	3006	6940	284	41
5	320	94	192	3012	6940	292	42
6	320	94	192	2999	6940	249	36
7	320	94	192	2987	6940	268	39
8	320	94	192	3017	6940	265	38
9	320	94	192	2987	6940	299	43
10	320	94	191	2979	6940	264	38
11	320	94	193	3012	6940	208	30
12	320	94	191	3017	6940	306	44
13	320	94	191	3004	6940	298	43
14	320	94	192	3003	6940	300	43
15	320	94	191	3015	6940	271	39
16	320	94	192	3014	6940	298	43
17	320	94	192	3023	6940	298	43
18	320	94	192	2991	6940	295	42
19	320	94	192	3003	6940	275	40
20	320	94	191	2996	6940	307	44
21	320	94	191	2987	6940	252	36
22	320	94	191	2998	6940	281	40
23	320	94	192	2994	6940	272	39
Mean (μ) - Std (σ)							$\mu = 40$ - $\sigma = 3$

Table 5
Concrete tensile strength from splitting tests on core specimens.

Test	Age	Dimensions		Weight	Cross-section	Maximum Load	f_{ct}
	[dd]	a [mm]	L mm]	[g]	[mm^2]	[kN]	[N/mm^2]
1	320	94	93	1481	6940	60	4,36
2	320	94	94	1497	6940	67	4,81
Mean (μ) – Std (σ)							$\mu = 4.27$ - $\sigma = 0.32$

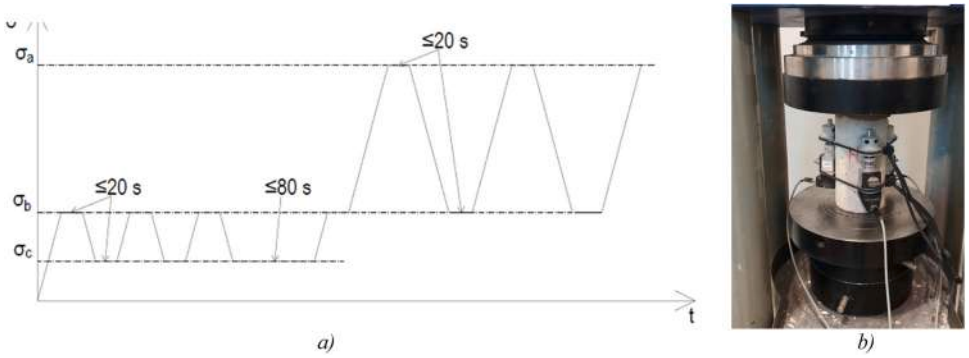

Fig. 9. : a) Loading protocol (σ-t) to estimate the concrete secant elastic modulus according to EN 12390–13 [47]. b) Picture of the specimen.

Table 6
Steel mechanical properties estimated through uniaxial tensile tests.

Test	Nominal Diameter [mm]	Initial Length [mm]	Cross section [mm^2]	Actual Diameter [mm]	Yielding Load [kN]	Ultimate Load [kN]	Final Length [mm]	f_y [N/mm^2]	f_u [N/mm^2]	A_{gl} [%]	μ_{fy} [N/mm^2]	μ_{fu} [N/mm^2]	σ_{fy} [N/mm^2]	σ_{fu} [N/mm^2]
d24a	24	100	440	24	228	282	113	504	624	13	504	625	0.0	0.5
d24b	24	100	442	24	228	283	112	504	625	12				
d18a	18	100	264	18	135	164	112	512	621	12	511	622	0.7	1.0
d18b	18	100	264	18	135	164	114	511	623	14				
d16a	16	100	197	16	106	125	111	538	631	11	539	631	1.1	0.5
d16b	16	100	198	16	107	125	110	540	632	10				
d14a	14	100	152	14	81	97	112	534	634	12	536	632	2.3	2.1
d14b	14	100	152	14	82	96	111	538	630	11				
d12a	12	100	112	12	62	74	108	554	660	8	548	655	5.9	4.5
d12b	12	100	111	12	60	73	109	543	651	9				
d8a	8	100	51	8	25	30	—	496	602	-	498	602	2.0	0.9
d8b	8	100	51	8	25	30	109	500	603	9				

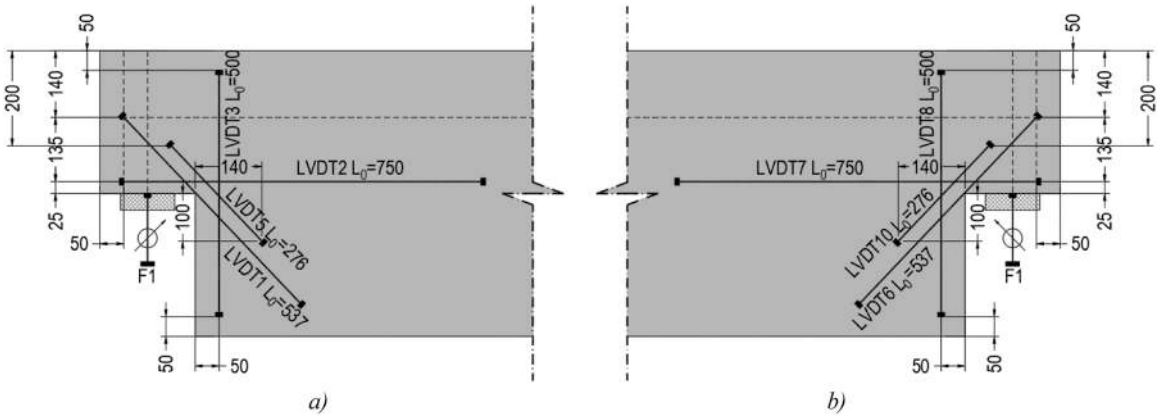

Fig. 10. Identification of the length and position of the linear variable differential transducers (LVDTs) a) Front face b) Backside face.

average value of the tensile strength. These results validate the accuracy in the casting of both beams and cylinder specimens.

The elastic modulus of the concrete is evaluated according to EN 12390–13 [47] (Fig. 9), where $\sigma_a = f_c/3$, with $f_c = 40$ N/mm^2 the average compressive strength on cubic specimens, σ_b in the range [10 % $f_c \div 15$ % f_c] and σ_a in the range [0.5 MPa $\div \sigma_b$]. The average value of the slopes of the last reloading branch of the stress-strain curves (σ-ε) gives the concrete secant elastic modulus, which holds 29045 N/mm^2.

2.4.2. Steel

The steel reinforcement is made of ribbed bars with a nominal yield strength of 450 MPa and a ductility grade C (B 450 C). All bar diameters used in the investigated dapped ends are considered. The results of the uniaxial tensile tests are listed in Table 6 in terms of yield strength (f_y), ultimate strength (f_u) and strain at maximum tensile force ($A_{gt,av}$ measured according to the procedure established in ISO 6892–122 [48]) for each rebar nominal diameter adopted. The symbols μ and σ identify the mean and the standard deviation of the experimental values, respectively.

2.5. Loading protocol and instrumentation

The specimens are loaded under displacement control at a constant stroke rate of 0.017 mm/s and are monotonically loaded beyond the peak load. The structural response of the dapped ends is monitored by arranging the instruments on both the right and left faces, along the main rebars (Fig. 10). To measure the crack opening displacements, linear variable differential transformers (LVDTs) are applied to all specimens: in the diagonal (LVDT5, LVDT10 and LVDT 11, LVDT6), horizontal (LVDT2, LVDT7), and vertical directions (LVDT3, LVDT8). The distance between the instrumented points is identified in Fig. 10, where the position of all LVDTs is also shown.

To measure the strains on the steel bars, strain gauges are applied on some specimens (T1–2A*, T2–2A, T3–2A and T3–2B) before the casting. The position of the strain gauges is shown in Fig. 11.

Three wire encoders (*F1*, *F2* and *F3*) are fixed to the ground to measure the vertical displacements (d_{F1}, d_{F2} and d_{F3}), respectively (Fig. 12). Data acquisition is performed at a rate of 1 Hz by an electronic measurement system connected to the loading machine. The measured vertical displacement of the target point (d_{F2}), at the bottom of the loaded section, has been corrected to account for the displacements d_{F1} and d_{F3} of the external supports:

$$d = d_{F2} - d_{F13} = d_{F2} - (d_{F3} + \Delta v) = d_{F2} - \left[d_{F3} + \left(\frac{d_{F1} - d_{F3}}{l} \right) a \right]$$

The net vertical displacement d of the target point is then adopted to draw the experimental load-displacement curves.

3. Results

3.1. Experimental results

The load-displacement curves are shown in Fig. 13 for all investigated specimens. The maximum external load P_u and corresponding displacement d_u are listed in Table 7 with a brief description of the failure mode.

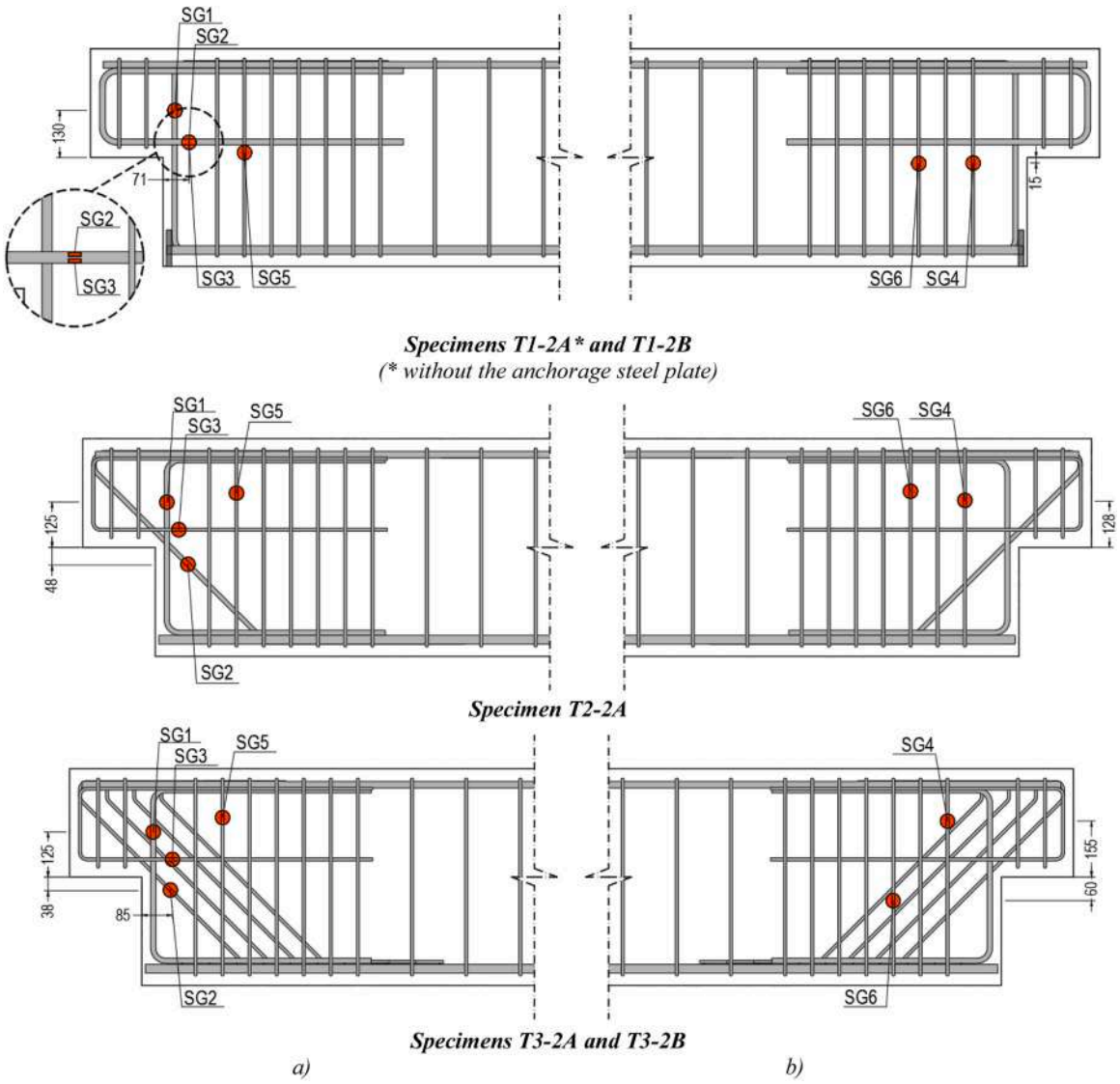

Fig. 11. Identification of the position of the i-th strain gauge (SG) a) Front face b) Backside face.

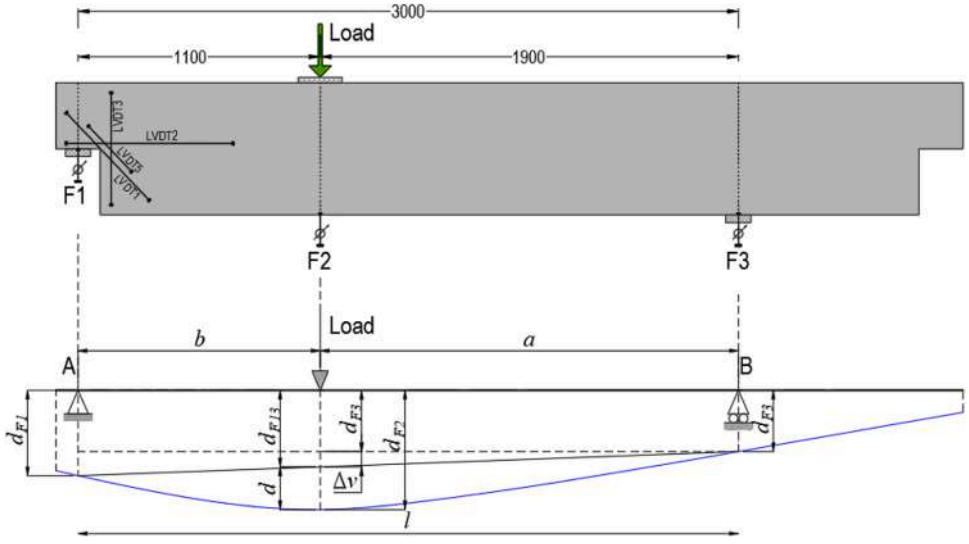

Fig. 12. : Specimen with identification of monitored displacements.

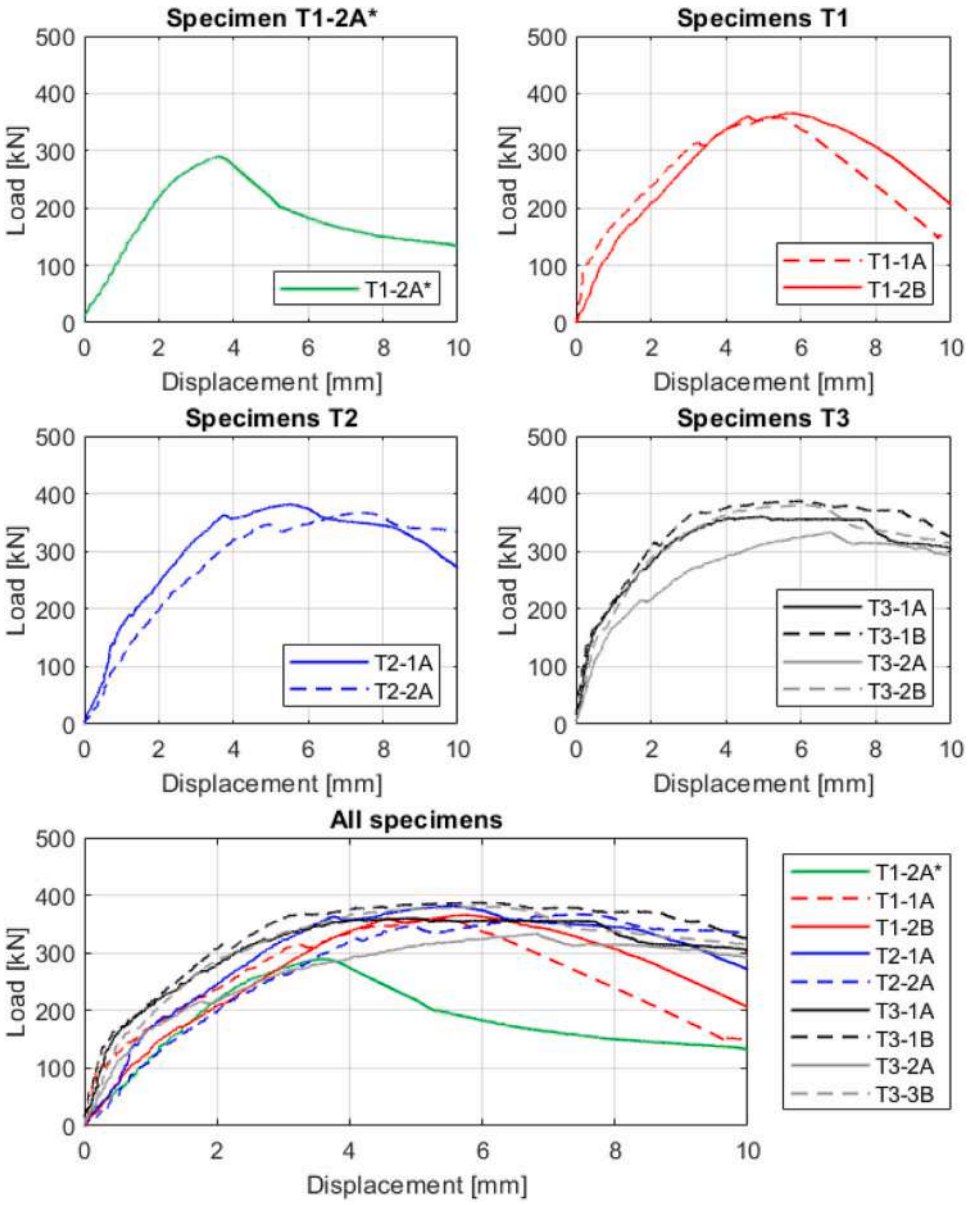

Fig. 13. Load-displacement (P-d) curves for all specimens.

Table 7
Maximum load (P_u), displacement (d_u) and failure mode of all specimens.

Specimen Type	Specimen label	Maximum Load P_u [kN]	Average of P_u $P_{u,avg}$ [kN]	Displacement d_u [mm]	Failure Mode
T1	T1 – 2A*	289	289	5.03	slippage of the bottom longitudinal reinforcement
	T1 – 1A	358	362	7.20	yielding of
	T1 – 2B	365		7.54	U reinforcement (2Φ16)
T2	T2 – 1A	381	374	7.37	yielding of U reinforcement (2Φ8)
	T2 – 2A	367		9.29	and diagonal bars (2Φ12)
T3	T3 – 1A	360	365	6.66	yielding of U reinforcement (2Φ8)
	T3 – 1B	386		7.84	and diagonal bars (6Φ8)
	T3 – 2A	333		8.44	
	T3 – 2B	380		8.03	

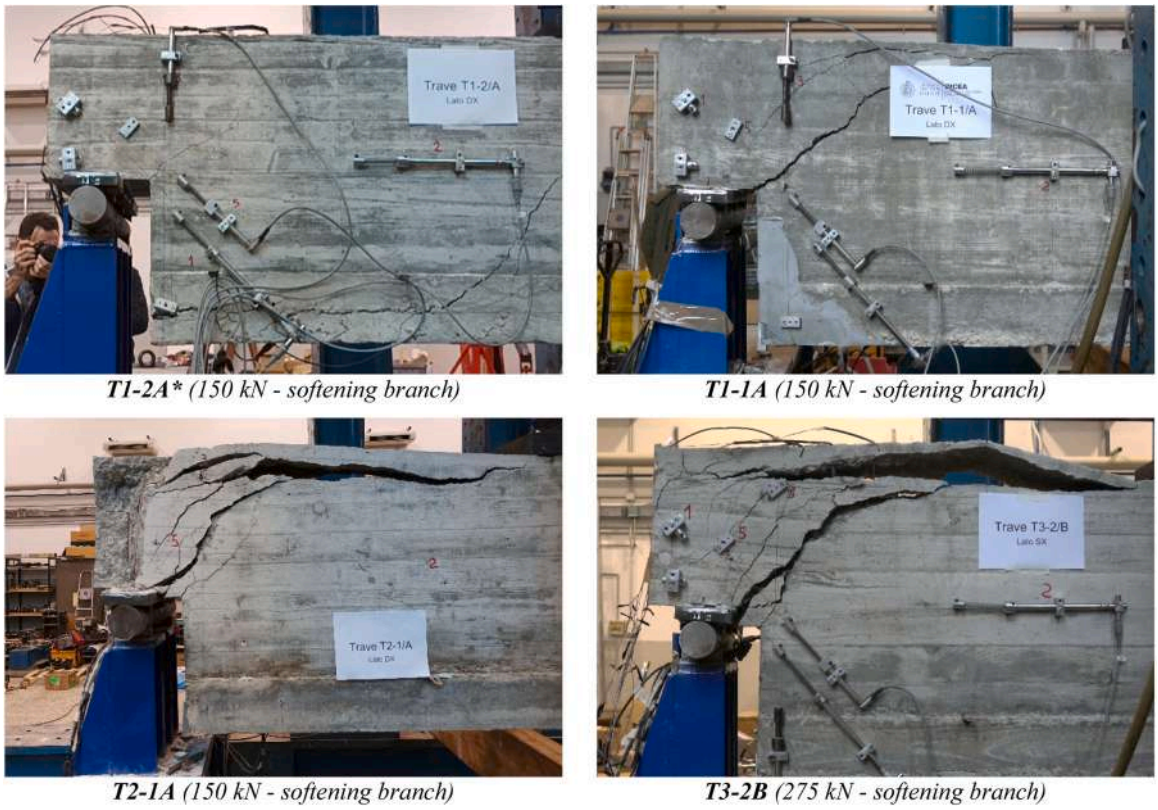

Fig. 14. Crack pattern observed in the softening branch.

Values of the maximum external load (P_u), listed in Table 7, show good repeatability in the tests, so the load-carrying capacity of specimens of the same type can be approximated with the average value ($P_{u,avg}$). Concerning specimens of type T3, the third specimen (T3–2A) undergoes premature damage and exhibits a lower ultimate load P_u= 333 kN than the other three specimens of the same type, probably due to a misalignment of the specimen T3–2A under the testing machine. Pictures of the specimens after failure are shown in Fig. 14 for clearness. The lesser load of 289 kN for specimen T1–2A* is due to the rebar slippage phenomenon, which is prevented in specimens T1–1A and T1–2B thanks to the additional anchorage plate at the end of the longitudinal bottom bars (Fig. 15).

The load-crack opening displacement (COD) curves are given in Fig. 16 for LVDTs shown in Fig. 10.

The markers in each graph indicate the load levels at which the pictures in Fig. 17 were taken (circle markers denote the following load values: 100, 150, 250 and 350 kN, the triangular marker corresponds to the maximum load).

The cracks start to develop from the inner corner of the nib, with an orientation at about 45° from the horizontal for all specimen types (T1, T2 and T3). Due to the slippage of the bottom longitudinal reinforcement of the beam, the specimen T1–2A* shows a different failure mode, characterized by a wide horizontal splitting crack, which extends diagonally upward at failure (Fig. 14).

The crack opening displacements are well identified for all specimens at the average maximum load $P_{u,avg}$ (Table 7); in specimens T2 and T3, CODs also highlight the beneficial effect provided by diagonal bars (Fig. 16). For those specimens, diagonal LVDTs (LVDT 6 and LVDT 1 and LVDT 10 and LVDT 5) achieve high displacement before the collapse (≥ 10 mm for specimens T3) and the load-displacement curves (*P-d*, Fig. 13) show an almost horizontal post-peak response, differently from specimens T1–1A and T1–2B. This is particularly evident in specimens T3 for LVDT 2 and LVDT 7, that is for the horizontal crack opening displacements, and can be explained with the presence of distributed diagonal bars, differently from other specimen types. The diffused cracks observed in specimens of type T3 could facilitate the timely detection of damaged half-joints during in situ inspections.

For each type of specimens, Table 8 lists average values of the crack opening displacements (COD) measured by LVDTs for different values of the ratio of the applied load P to the maximum average load $P_{u,avg}$. For specimens of type T1 experimental data are averaged from tests T1–1A and T1–2B (T1–2A* is not considered due to the premature slippage of bottom longitudinal bars), for specimens T2 data are averaged from both tests T2–1A and T2–2A, and for specimens T3 data are averaged from all four tests. Specimens T2 and T3 are characterized by reduced cracks at service load compared to specimens T1 (P = 250 kN, Table 8), as shown by lower displacements registered by diagonal LVDTs (LVDT 6 and LVDT 1 and LVDT 10 and LVDT 5) before the ultimate load.

The load-strain curves of specimens T1–2A* , T1–2B, T2–2A, T3–2A and T3–2B are drawn in Fig. 18 for the strain gauges shown in Fig. 11. The values of crack opening strains (COS) are listed in Table 9.

For specimen T1–2A* , the external load increases up to 250 kN when a splitting horizontal crack begins to open at the bottom longitudinal bars of the beam and the diagonal crack is approximately 0.9 mm. For a load of 283 kN, the strain gauge SG3, placed on the bottom of the U-bar (Φ16), reaches the yield strain (Fig. 18), while the strain gauge SG2, located on the top of the same bar in the same cross-section as SG3, remains in the elastic range. The different values of strains in the top and bottom fibers of the bar cross-section suggest the presence of a “dowel action” in the bar. At the maximum load of 289 kN, the horizontal crack extends for 600 mm along the bottom bars (Fig. 15) with a maximum width of 1.2 mm, then diagonally extends upward.

Fig. 15. a) Failure mode of specimen T1–2A* with diagonal crack and identification of the slippage of the bottom longitudinal bars (yellow arrows). b) View of specimen T1–2B in an upside-down position before launching (left) and on the testing machine (right): the arrow identifies the anchorage plate.

Regarding specimen T1–2B, the beneficial effect provided by the anchorage plate, connected to the bottom steel bars of the beam, is highlighted by a greater load-carrying capacity than specimen T1–2A* . The load increases up to about 250 kN when a diagonal crack begins to open (approximately at 45°) starting from the internal corner of the nib. At a load of about 360 kN, the crack extends to the concrete cover at the top of the beam.

Regarding specimen T2–2A, the load increases up to about 100 kN when a diagonal crack begins to open at the internal corner of the nib. Once the load reaches about 323 kN, the U-shaped bar (Φ8) yields as recorded by the SG3 strain gauge. At approximately 335 kN the diagonal bar (Φ12) yields as monitored by SG2. At around a load of 337 kN, the yield strength of the vertical bar Φ14 is achieved (see strain gauge SG1 results in Fig. 18). The load continues to increase to a maximum value of approximately 366 kN. As the imposed displacement increases, the load begins to decrease. At a vertical displacement of 11.95 mm, in the softening branch, the first stirrup (Φ8) yields as confirmed by SG4.

Concerning specimen T3–2B, the load increases steadily up to approximately 148 kN, when a diagonal crack begins to open at the internal corner of the nib. The crack is inclined at 45° and its width increases as the load increases. Once the load reaches about 296 kN, the yielding at the diagonal bar is recorded by SG2 (Fig. 18). Subsequently, at around 327 kN, the U-shaped horizontal bar (Φ8) yields as recorded by SG3. The load continues to increase to a maximum of 379 kN.

In all types of specimens, strain gauges SG5 and SG6 are scarcely activated, particularly in specimen T1–2A* and all four specimens of type T3. An appreciable activation of the SG5 and SG6 strain gauges is observed in test T2–2A, where the strain reaches 1.27 ‰ in the second stirrup (SG5) and 0.11 ‰ in the third stirrup (SG6), while in test T1–2B a strain of 1.06 ‰ is reached in the second stirrup and of 0.58 ‰ in the third stirrup. However, all these values recorded by the strain gauges SG5 and SG6 are lower than the value of the stirrup yield strain of 2.4 ‰.

4. Discussion

The maximum load recorded in experimental tests is similar for all specimens (see Table 7) with an average of 367 kN and a coefficient of variation V= 0.018. The premature damage due to the absence of the anchorage plate of the bottom longitudinal bars for test T1–2A* involves a lower maximum load (289 kN).

Fig. 20 shows the graphs of vertical and horizontal bar forces for all tested specimens equipped with strain gauges. As strain gauges were not active till the end of the tests, graphs were drawn until the strain gauges worked. The notation for the selected bar forces is shown in Fig. 19. In the graphs of vertical bar forces, the dashed line corresponds to the total shear force on the nib V_{nib}, therefore the difference between the dashed line and the upper continuous line represents the vertical force taken by the concrete and dowel action of rebars.

The higher bar forces are recorded at the re-entrant corner. Initially, in all tests, the shear force seems to be completely supported by the concrete in tension, therefore the curves of vertical forces in the reinforcement are almost horizontal in the first branch. The test T1–2A* is an exception because a crack was present in the specimen before the test started, so the curves are linear from the beginning. As the load increases and cracks form, the relative contribution of each force component varies. For the specimens of type T1, the vertical force is mainly

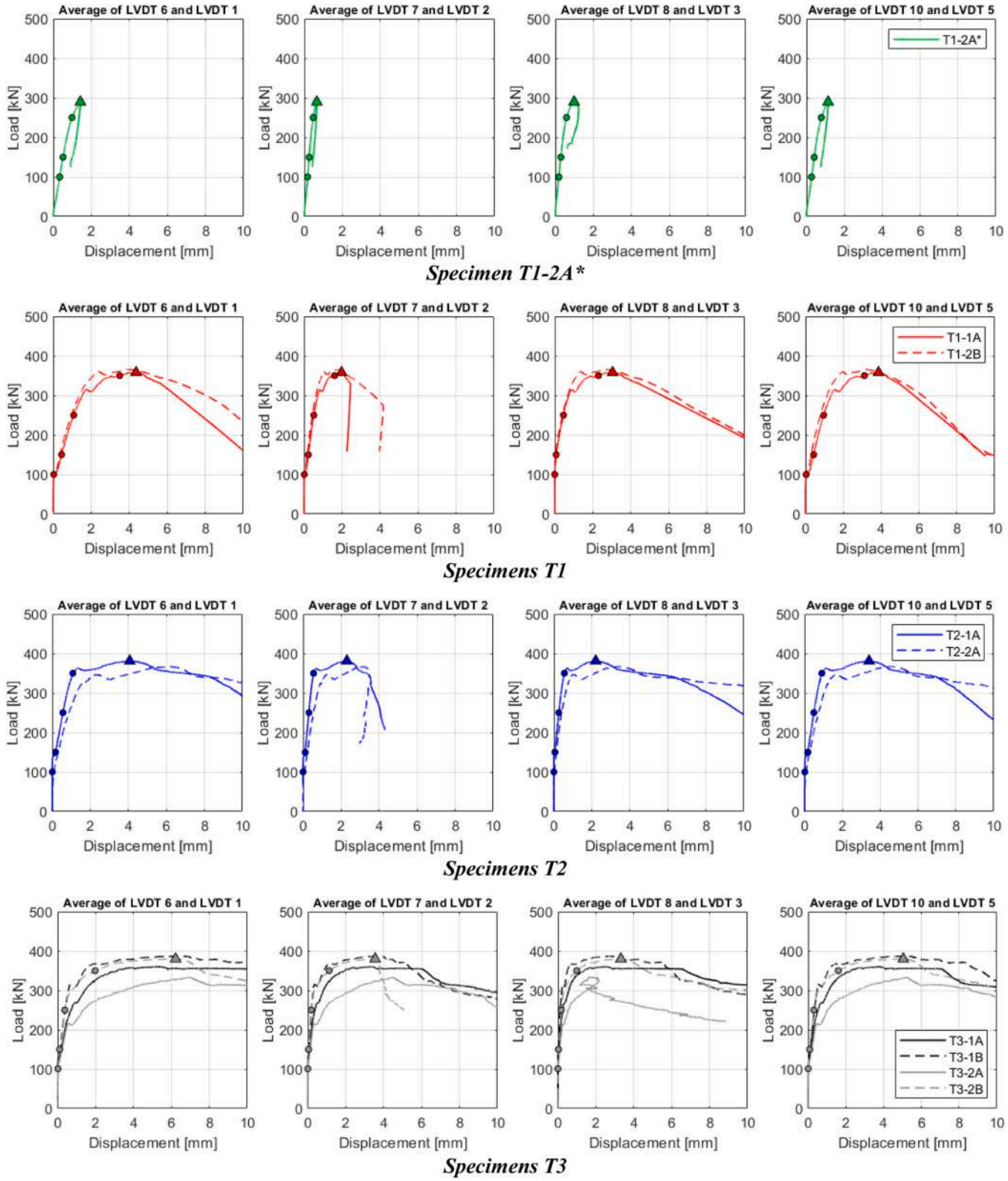

Fig. 16. Crack opening displacement for all LVDTs shown in Fig. 10.

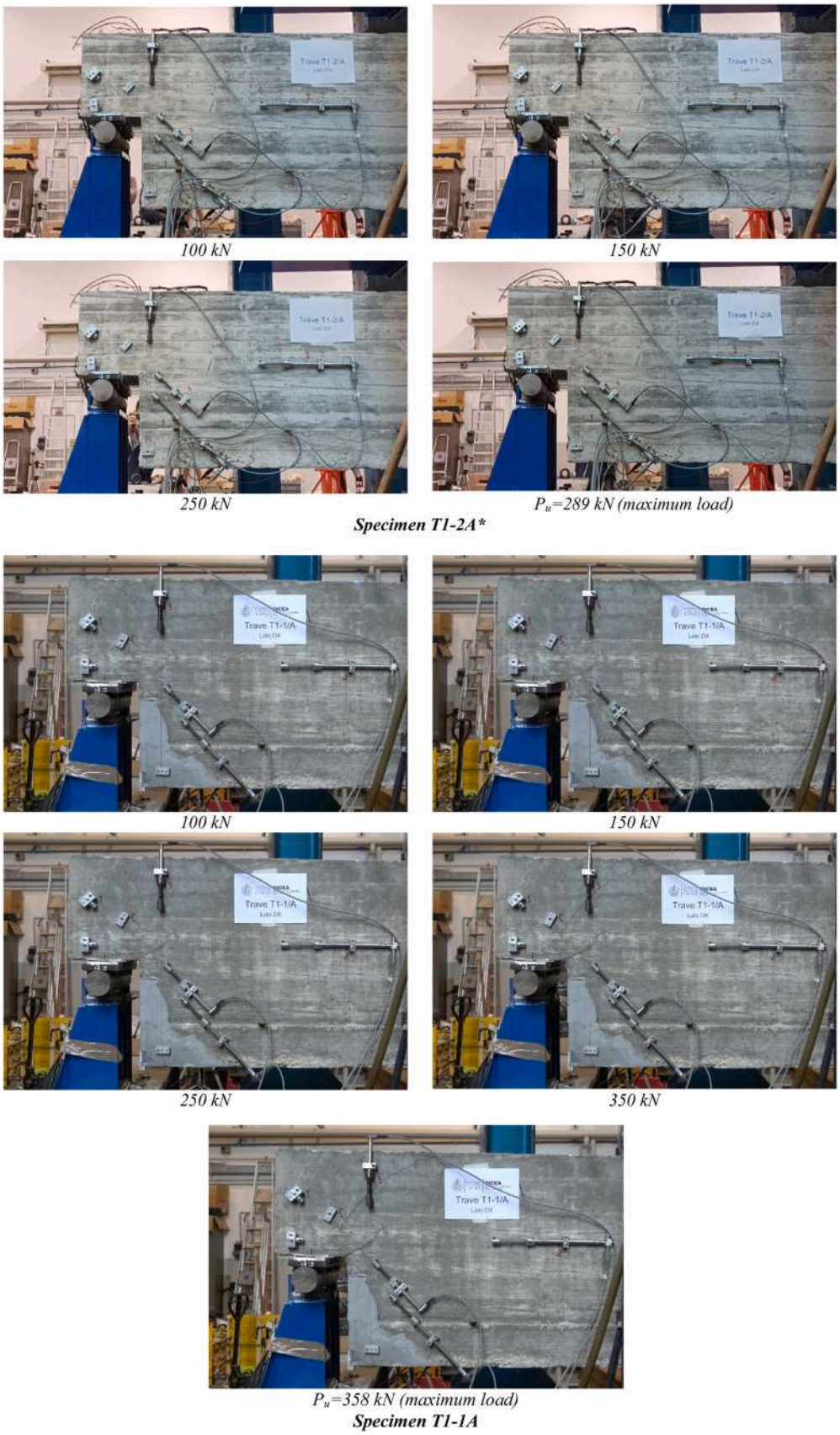

Fig. 17. Crack pattern at different levels of the applied external load.

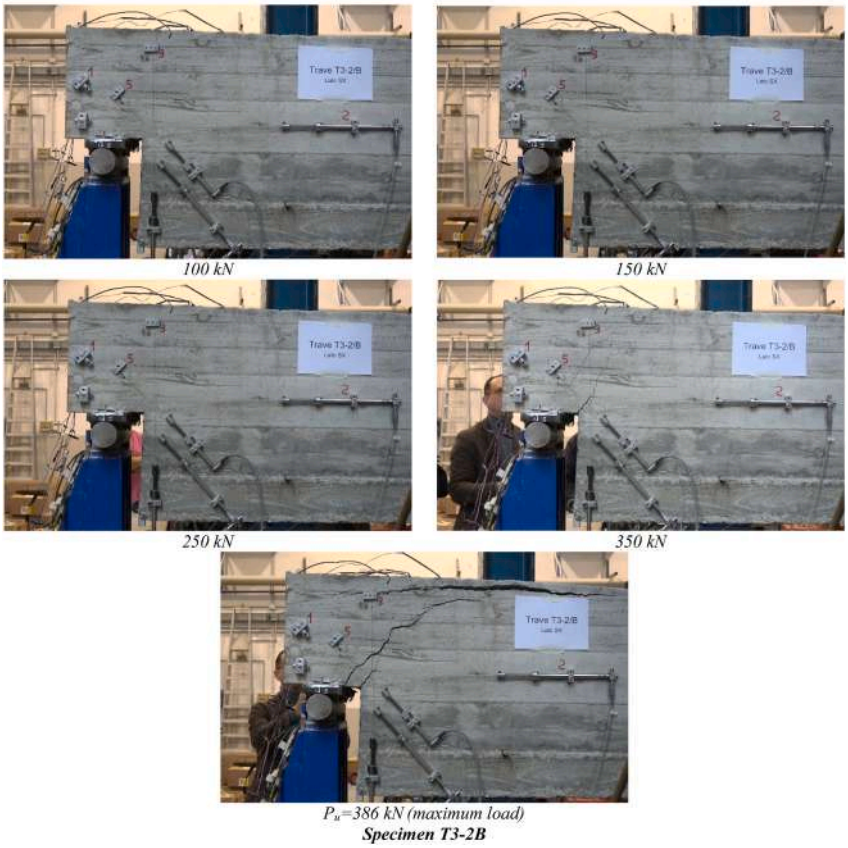

Fig. 17. (*continued*).

Table 8
Average values of crack opening displacements (COD) [mm] for several levels of the external load (P) [kN].

Specimen	P [kN]	100	150	250	350	$P_{u,avg}$ (1)
T1 – 2A*	$P/P_{u,avg}$	35 %	52 %	87 %	\\	100 %
(one test)	LVDT 1 –6	0,34	0,51	0,98	\\	1,43
	LVDT 2 –7	0,17	0,25	0,47	\\	0,66
	LVDT 3 –8	0,18	0,29	0,59	\\	0,98
	LVDT 5 –10	0,27	0,41	0,79	\\	1,14
T1 – 1A	$P/P_{u,avg}$	28 %	41 %	69 %	97 %	100 %
T1 – 2B	LVDT 1 –6	0,03	0,45	1,08	3,50	4,36
(two tests)	LVDT 2 –7	0,02	0,23	0,52	1,61	1,98
	LVDT 3 –8	0,00	0,08	0,46	2,30	3,05
	LVDT 5 –10	0,04	0,43	0,97	3,11	3,86
T2 – 1A	$P/P_{u,avg}$	27 %	40 %	67 %	94 %	100 %
T2 – 2A	LVDT 1 –6	0,00	0,18	0,56	1,08	4,07
(two tests)	LVDT 2 –7	0,00	0,11	0,31	0,55	2,30
	LVDT 3 –8	0,00	0,06	0,26	0,56	2,21
	LVDT 5 –10	0,01	0,17	0,49	0,91	3,41
T3 – 1A	$P/P_{u,avg}$	27 %	41 %	69 %	96 %	100 %
T3 – 1B	LVDT 1 –6	0,02	0,10	0,38	1,98	6,22
T3 – 2A	LVDT 2 –7	0,00	0,04	0,18	1,12	3,55
T3 – 2B	LVDT 3 –8	0,00	0,03	0,17	0,99	3,32
(four tests)	LVDT 5 –10	0,01	0,09	0,31	1,60	5,04

(1) $P_{u,avg}$(T1-2A*)= 289 kN - $P_{u,avg}$(T1)= 362 kN - $P_{u,avg}$(T2)= 374 kN - $P_{u,avg}$(T3)= 365 kN

transferred by the vertical ϕ14 bars ($V_{\varphi 14}$). As expected, the force on stirrups is related to the diagonal crack growth, which starts at the re-entrant corner and continues to grow crossing the stirrups, from the closer to the farther.

In specimens of types T2 and T3, the greatest contribution to the maximum shear force in the nib is given by the diagonal bars (see the vertical component force V_{diag} in Fig. 20).

The total force supported by rebars is almost equal to the shear force acting on the nib, with very little difference between the dashed line and the upper continuous line corresponding to the sum of the vertical forces on rebars. This difference is greater for specimens T3–2A and T3–2B, because the other three diagonal bars participated in the resistant mechanism but were not equipped with strain gauges so their strains were not measured.

In addition, Fig. 20 allows for identifying the number of stirrups activated in the resistant mechanism, after the vertical ϕ14 bars (one stirrup for specimens T1 and two stirrups for specimens T2 and T3).

In detail, in test T1–2A* , when a maximum support reaction force V_{nib} of 183 kN is reached (see Fig. 20), the total force in the U-bars is 157 kN, the steel vertical forces are almost fully taken by vertical bars φ14 (80 %) and for a limited amount by the first stirrup (5.2 %).

During test T1–2B, once the support reaction V_{nib} has reached the value of 220 kN (see Fig. 20), the force in the U-bars stopped being registered as SG3 went out of service (see also Fig. 18). Vertical bars ϕ14 carry approximately 77 % of the vertical reaction V_{nib}, with 14.6 % carried by the first stirrup and 3.5 % by the second stirrup, while the third stirrup is scarcely activated.

For test T2–2A, at a support reaction value V_{nib}= 208 kN, a total horizontal force of 124.5 kN is carried by the reinforcement. This force is divided into 46.7 % carried by the U-bars (58.1 kN) and 53.3 % carried by the diagonal bar (66.4 kN). The proportions for the total vertical reinforcement force of 200.3 kN are 33.1 % for the diagonal bar (66.2 kN), 47.3 % for vertical bars ϕ14 (94.8 kN), 13.2 % for the first stirrup (26.5 kN), 5.8 % for the second stirrup (11.6 kN), and 0.6 % for the third stirrup (1.2 kN). At lower load levels, most of the vertical reinforcement force is carried by the two vertical bars ϕ14 and the diagonal bars. The first stirrup does not provide a significant contribution to the distribution of the overall vertical force until V_{nib}= 65 kN. The second stirrup is activated at V_{nib}= 102 kN; at this load level, the crack initiated at the re-entrant corner begins to propagate and crosses the third stirrup.

For test T3–2A, at a support reaction value V_{nib}= 132.9 kN, a total horizontal force of 61.9 kN is registered in the reinforcement. This force is divided into 49.9 % carried by the U-bars (30.9 kN) and 50.1 % carried by the first diagonal bar (31 kN). The proportions for the total vertical reinforcement force of 76.5 kN are 40.4 % for the first diagonal bar (30.9 kN), 46.4 % for the vertical bars ϕ14 (35.5 kN), 10.3 % for the first stirrup (7.9 kN), 2.1 % for the second stirrup (1.6 kN), and 0.8 % for the third stirrup (0.6 kN). At lower load levels, most of the vertical reinforcement force is carried by the first diagonal bar and vertical bars ϕ14. The first stirrup does not provide a significant contribution to the distribution of the overall vertical force until V_{nib}= 73 kN. The second stirrup is activated at V_{nib}= 86 kN.

During test T3–2B, once the support reaction V_{nib} reaches the value of 212.7 kN, a total horizontal force of 100.4 kN is absorbed by the reinforcement. This force is divided into 56.4 % carried by the U-bars (56.6 kN) and 43.6 % carried by the first diagonal bar (43.8 kN). The proportions for the total vertical reinforcement force of 145.1 kN are 30.0 % for the first diagonal bar (43.5 kN), 46.2 % for vertical bars ϕ14 (67.1 kN), 16.8 % for the first stirrup (24.4 kN), 7.0 % for the second stirrup (10.1 kN), and 0.0 % for the third stirrup. At lower load levels, most of the vertical reinforcement force is carried by the first diagonal bar and vertical bars ϕ14. The first stirrup does not provide a significant contribution to the overall vertical force until V_{nib}= 85 kN. The second stirrup is activated at V_{nib}= 96 kN.

Results also suggest that thanks to the presence of diagonal bars (specimens T2 and T3), a reduced crack pattern is registered under service load and the load-displacement curves exhibit an appreciable ductile horizontal branch, differently from specimens T1 (Fig. 13). The average values of the crack opening displacements (CODs) measured by LVDTs for different ratios of the applied load P are shown in Fig. 21 for all specimens (T1 - T2 - T3).

Observing the crack pattern (Fig. 17), it is evident that the wider cracks developed at the inner corner of the nib, and they are inclined at about 45° (perpendicular to LVDT 1–6 and LVDT 5–10). Fig. 21 highlights that the CODs are reduced for specimens T2 and T3 under service loads, in the range between 100 kN and 350 kN. At the same time, at the average maximum load ($P_{u,avg}$), the crack opening displacements (CODs) for specimens T3 - equipped with distributed diagonal bars - increase and a greater ultimate displacement is reached.

5. Conclusions

An experimental campaign was conducted to evaluate the influence of reinforcement layout on the structural performance of RC dapped ends, focusing on the cracking pattern, the distribution of forces in steel bars and post-peak behavior. All specimens have the same geometrical dimensions and are made with the same materials. Three different reinforcement layouts were chosen for comparison: Type 1 with only horizontal U-bars and vertical bars; Type 2 with horizontal U-bars, vertical bars, and one layer of diagonal bars; and Type 3, like Type 2 but with four layers of diagonal bars. Once the reinforcement layouts were established, the bar diameters were sized to guarantee about the same load-bearing capacity for all three types of specimens, which were then tested until failure.

The experimental failure load of specimens of type T1 is very close to the value predicted using the S&T model, confirming that the modified version of Truss 1 model can provide a reliable evaluation of the ultimate load in dapped ends equipped with horizontal and distributed vertical bars. Similarly, the experimental failure load of specimens of types T2 and T3 is also very close to the numerical value predicted with the preliminary FE model, although simple elastoplastic constitutive laws for materials were used.

The experimental results allow for some interesting conclusions about the force distribution among the steel rebars, the cracking pattern and the post-peak behavior.

In all specimens, the first crack arises at the inner corner of the nib at

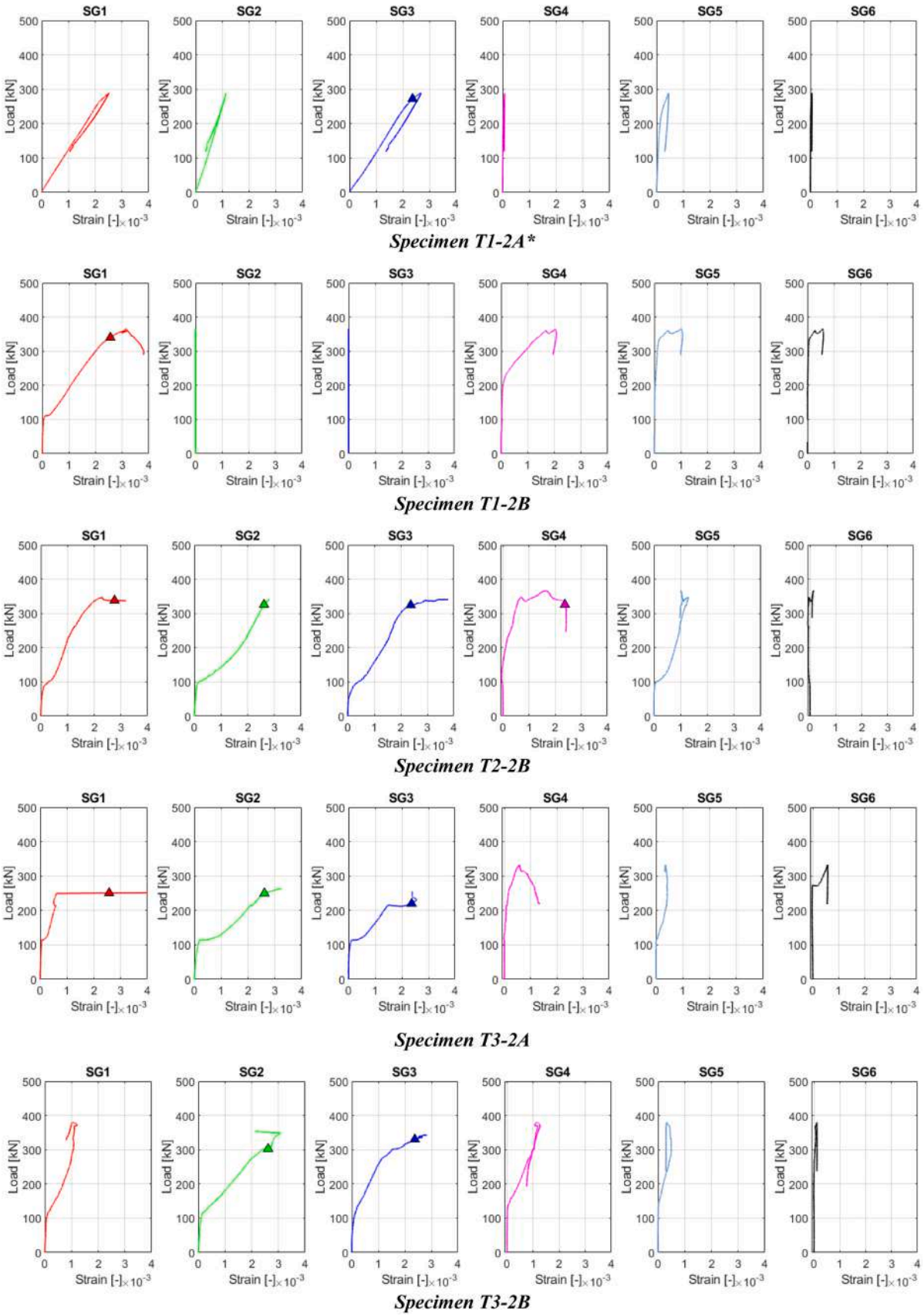

Fig. 18. : Load-strain curves for all strain gauges (Fig. 11) with the identification (triangle) of the yielding strain.

Table 9
Average values[(1)] of crack opening strains (COS) [‰] for several levels of the external load P [kN].

Specimen	P [kN]	100	150	250	350	$P_{u,avg}$
T1 – 2A*	P/P_u	35 %	52 %	87 %	\\	100 %
(one test)	LVDT 1 –6	0,64	0,96	1,83	\\	2,65
	LVDT 2 –7	0,23	0,34	0,62	\\	0,88
	LVDT 3 –8	0,37	0,58	1,17	\\	1,95
	LVDT 5 –10	0,99	1,50	2,87	\\	4,16
T1 – 1A	$P/P_{u,avg}$	28 %	41 %	69 %	97 %	100 %
T1 – 2B	LVDT 1 –6	0,06	0,83	2,00	6,51	8,11
(two tests)	LVDT 2 –7	0,03	0,31	0,69	2,15	2,64
	LVDT 3 –8	0,00	0,16	0,92	4,57	6,05
	LVDT 5 –10	0,14	1,57	3,51	11,32	14,05
T2 – 1A	$P/P_{u,avg}$	27 %	40 %	67 %	94 %	100 %
T2 – 2A	LVDT 1 –6	0,01	0,33	1,04	2,01	7,57
(two tests)	LVDT 2 –7	0,00	0,15	0,41	0,74	3,07
	LVDT 3 –8	0,00	0,12	0,52	1,11	4,38
	LVDT 5 –10	0,05	0,63	1,78	3,33	12,40
T3 – 1A	$P/P_{u,avg}$	27 %	41 %	69 %	96 %	100 %
T3 – 1B	LVDT 1 –6	0,04	0,19	0,71	3,67	11,55
T3 – 2A	LVDT 2 –7	0,00	0,05	0,24	1,50	4,74
T3 – 2B	LVDT 3 –8	0,00	0,06	0,35	1,96	6,59
(four tests)	LVDT 5 –10	0,03	0,31	1,11	5,83	18,34

[(1)] Average values of two LVDTs positioned on opposite faces - P_u(T1-2A*)= 289 kN - $P_{u,avg}$(T1)= 362 kN - $P_{u,avg}$(T2)= 374 kN - $P_{u,avg}$(T3)= 365 kN

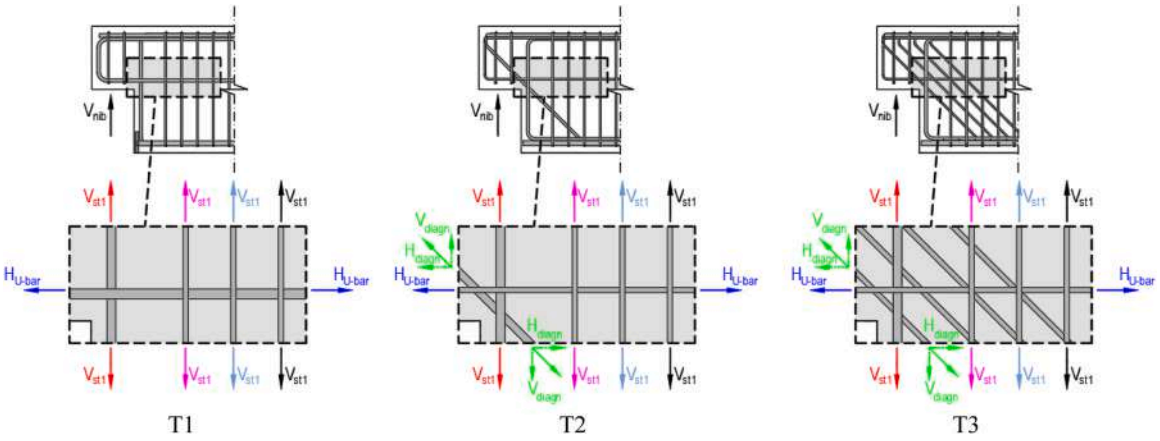

Fig. 19. Identification of the forces label on rebars for all tested specimens with strain gauges.

a load level corresponding to 30 % of the maximum load for T1 specimens and 40 % of the maximum load for T2 and T3 specimens; in all specimens the first crack is oriented at about 45° to the longitudinal axis. In specimens of types T2 and T3 diagonal bars allow for the formation of additional diagonal cracks, differently from specimens of type T1, where only a secondary diagonal crack opens. In general, diagonal bars enhance serviceability by minimizing crack width and slowing the rate of crack development. Moreover, the load-displacement curves of T2 and T3 specimens exhibit an almost horizontal ductile post-peak branch, particularly in specimens of type T3. The behavior of T2 and T3 specimens in both the cracked and post-peak phase can surely facilitate the timely detection of damaged dapped ends during in situ inspections.

Experimental results also highlight how the different steel rebars contribute to the resistance of the specimens. In specimens of Type 1 the two vertical bars ϕ14 carry approximately 77 % of the vertical reaction, while the first stirrup carries about 15 %, the second stirrup carries only 4 %, and the third stirrup is practically unloaded. In specimens of Type 2, at low load levels, most of the vertical reinforcement force is carried by the two vertical bars (ϕ14) together with the diagonal bars. As the external load increases, a redistribution of forces occurs, involving the first and second stirrups in the resisting mechanism. Near the failure load, 47 % of the vertical force is carried by the two 14 mm bars, 33 % by the diagonal bars, and 13 % and 6 % by the first and second stirrups, respectively. In specimens of Type 3, at low load levels, most of the vertical reinforcement force is carried by the first layer of diagonal bars and 14 mm vertical bars. Approaching the failure load, 30 % of the total vertical force in the reinforcement is carried by the first layer of diagonal bars (43.5 kN), 46 % by vertical bars (ϕ14), 17 % by the first stirrup, and 7 % by the second stirrup, with the third stirrup remaining unloaded.

The distribution of forces among steel rebars confirms that a S&T model where the hanger tie is formed by all vertical rebars grouped together in their center of gravity is not appropriate, as expected, because it does not consider the actual number of rebars involved in the resistant mechanism. Strain gauge data clearly show that stirrups are not loaded uniformly and the more distant from the nib are almost unloaded.

In the continuation of the research, more refined non-linear finite element models are being developed using the experimental values of the material mechanical parameters, not available at the time of dimensioning the specimens, to simulate the experimental load-displacement curves, cracking patterns, damaged zones and post-peak behavior, along with the distribution of forces in all steel rebars.

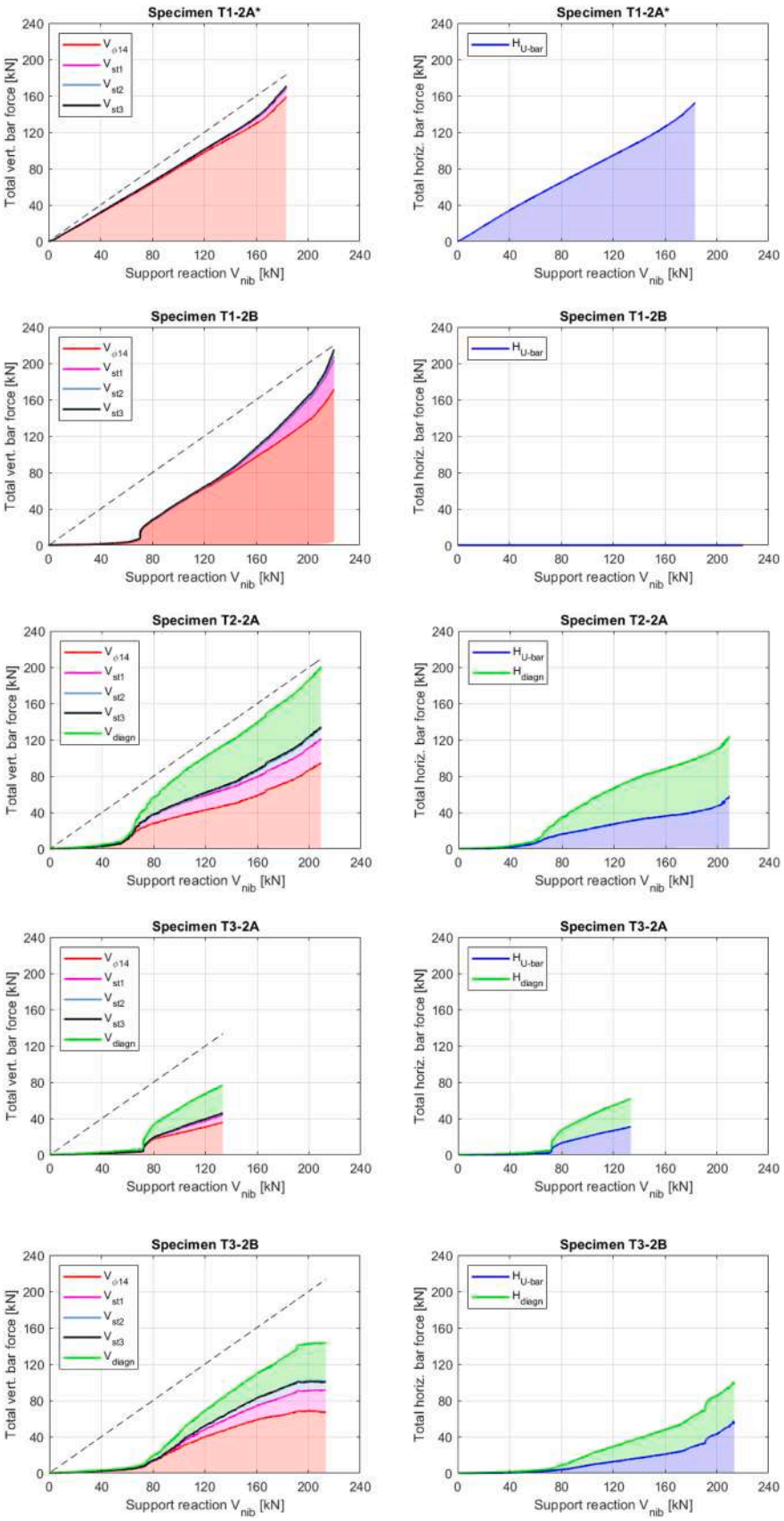

Fig. 20. Total forces in the vertical (left) and horizontal (right) bars for all tested specimens equipped with strain gauges.

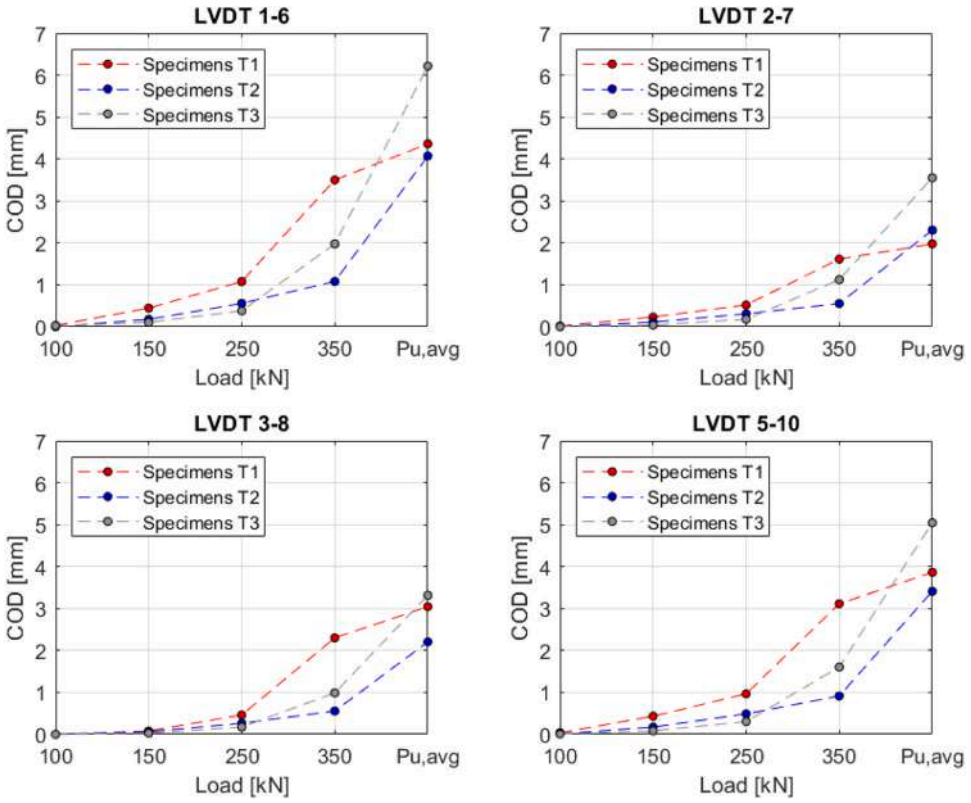

Fig. 21. *: Average values of crack opening displacements registered by all LVDTs of* Fig. 10 *at varying the* ***external load (P) [kN].***

Conflict of Interest and Authorship Conformation Form

Please check the following as appropriate:

- o All authors have participated in (a) conception and design, or analysis and interpretation of the data; (b) drafting the article or revising it critically for important intellectual content; and (c) approval of the final version.
- o This manuscript has not been submitted to, nor is under review at, another journal or other publishing venue.
- o The authors have no affiliation with any organization with a direct or indirect financial interest in the subject matter discussed in the manuscript

CRediT authorship contribution statement

All the authors contributed to development of the research, the discussion of results and preparation of the final manuscript.

CRediT authorship contribution statement

Giovanni Menichini: Writing – original draft, Validation, Methodology, Investigation, Data curation, Conceptualization. **Salvatore Giacomo Morano:** Writing – original draft, Validation, Supervision, Methodology, Investigation, Data curation, Conceptualization. **Federico Gusella:** Writing – original draft, Validation, Methodology, Investigation, Data curation, Conceptualization. **Maurizio Orlando:** Writing – original draft, Supervision, Project administration, Methodology, Investigation, Funding acquisition, Data curation, Conceptualization.

Declaration of Competing Interest

The authors declare that they have no known competing financial interests or personal relationships that could have appeared to influence the work reported in this paper.

Data availability

Data will be made available on request.

Acknowledgments

The study presented was conducted as part of the program of activities carried out within the agreement between the ReLUIS Interuniversity Consortium and the Superior Council of Public Works stipulated pursuant to art. 3 of the Decree of the Minister of Infrastructure no. 578 of 17 December 2020; however, this publication does not necessarily reflect the Council's position and assessments. The authors express their gratitude to UNICAL SpA, particularly to Dr Marco Francini, for supplying the concrete used in casting the beams.

References

[1] Johnson PM, Couture A, Nicolet R. Report of the commission of inquiry into the collapse of a portion of the de la Concorde overpass. Gov Que 2007.
[2] di Prisco M, Colombo M, Martinelli P. Structural aspects of the collapse of a RC half-joint bridge: case of the annone overpass. J Bridg Eng 2023;28:5023007. https://doi.org/10.1061/JBENF2.BEENG-6063.
[3] Mata-Falcón J, Pallarés L, Miguel PF. Proposal and experimental validation of simplified strut-and-tie models on dapped-end beams. Eng Struct 2019;183:594–609. https://doi.org/10.1016/j.engstruct.2019.01.010.
[4] Mitchell D, Collins MP. Revision of Strut-and-tie Provisions in the AASHTO LRFD Bridge Design Specifications. Dorion,; 2013.
[5] Moreno-Martínez JY, Meli R. Experimental study and numerical simulation of the behaviour of concrete dapped-end beams. Int J Eng Model 2013;26:15–25.
[6] Atta A, Taman M. Innovative method for strengthening dapped-end beams using an external prestressing technique. Mater Struct 2016;49:3005–19. https://doi.org/10.1617/s11527-015-0701-8.
[7] Mohammed BS, Aswin M, Liew MS. Prediction of failure load of RC and R-ECC dapped-end beams. Case Stud Constr Mater 2020;13:e00433. https://doi.org/10.1016/j.cscm.2020.e00433.

[8] Zamri NF, Mohamed RN, Elliott KS. Shear capacity of precast half-joint beams with steel fibre reinforced self-compacting concrete. Constr Build Mater 2021;272:121813. https://doi.org/10.1016/j.conbuildmat.2020.121813.
[9] Özkılıç YO, Yazman Ş, Aksoylu C, Arslan MH, Gemi L. Numerical investigation of the parameters influencing the behavior of dapped end prefabricated concrete purlins with and without CFRP strengthening. Constr Build Mater 2021;275:122173. https://doi.org/10.1016/j.conbuildmat.2020.122173.
[10] Don W, Suryanto B, Tambusay A, Suprobo P. Forensic assessments of the influence of reinforcement detailing in reinforced concrete half-joints: a nonlinear finite element study. Structures 2022;38:689–703. https://doi.org/10.1016/j.istruc.2022.02.029.
[11] Flores Ferreira K, Rampini MC, Zani G, Colombo M, di Prisco M. Experimental investigation on the use of fabric-reinforced cementitious mortars for the retrofitting of reinforced concrete dapped-end beams. Struct Concr 2023. https://doi.org/10.1002/suco.202200743.
[12] Desnerck P, Lees JM, Morley CT. The effect of local reinforcing bar reductions and anchorage zone cracking on the load capacity of RC half-joints. Eng Struct 2017;152:865–77. https://doi.org/10.1016/j.engstruct.2017.09.021.
[13] Clark LA, Thorogood P. Serviceability behaviour of reinforced concrete half joints. Struct Eng 1988;66.
[14] Moreno-Martínez JY, Meli R. Experimental study on the structural behavior of concrete dapped-end beams. Eng Struct 2014;75:152–63. https://doi.org/10.1016/j.engstruct.2014.05.051.
[15] Muttoni A, Schwartz J, Thürlimann B. Design of Concrete Structures with Stress Fields. Springer Science & Business Media,; 1996.
[16] Wang Q, Guo Z, Hoogenboom PCJ. Experimental investigation on the shear capacity of RC dapped end beams and design recommendations. Struct Eng Mech 2005;21:221.
[17] Lu W-Y, Lin I-J, Yu H-W. Behaviour of reinforced concrete dapped-end beams. Mag Concr Res 2012;64:793–805. https://doi.org/10.1680/macr.11.00116.
[18] Lu W-Y, Chen T-C, Lin I-J. Shear strength of reinforced concrete dapped-end beams with shear span-to-depth ratios larger than unity. J Mar Sci Technol 2015;23:5.
[19] Boothman D, Leckie S, MacGregor I, Brodie A. Assessment of concrete half-joints using non-linear analysis. Proc Inst Civ Eng - Bridg Eng 2008;161:141–50. https://doi.org/10.1680/bren.2008.161.3.141.
[20] Angotti F, Guiglia M, Marro P, Orlando M. In: Angotti F, Guiglia M, Marro P, Orlando M, editors. Strut-And-Tie Models BT - Reinforced Concrete with Worked Examples. Cham: Springer International Publishing; 2022. p. 587–691. https://doi.org/10.1007/978-3-030-92839-1_10.
[21] Rajapakse C, Degée H, Mihaylov B. Assessment of failure along re-entrant corner cracks in existing RC dapped-end connections. Struct Eng Int 2021;31:216–26. https://doi.org/10.1080/10168664.2021.1878975.
[22] Yang K-H, Ashour AF, Lee J-K. Shear strength of reinforced concrete dapped-end beams using mechanism analysis. Mag Concr Res 2011;63:81–97. https://doi.org/10.1680/macr.9.00006.
[23] Menichini G, Gusella F, Orlando M. Methods for evaluating the ultimate capacity of existing RC half-joints. Eng Struct 2024;299:117087. https://doi.org/10.1016/j.engstruct.2023.117087.
[24] Xinchen Z, Bing L. Seismic performance of interior reinforced concrete beam–column joint with corroded reinforcement. J Struct Eng 2022;148:4021275. https://doi.org/10.1061/(ASCE)ST.1943-541X.0003255.
[25] Xia Y, Langelaar M, Hendriks MAN. Optimization-based strut-and-tie model generation for reinforced concrete structures under multiple load conditions. Eng Struct 2022;266:114501. https://doi.org/10.1016/j.engstruct.2022.114501.
[26] EN 1992–1-1. Eurocode 2: Design of concrete structures. Part 1–1: General rules and rules for buildings. Brussels, Belgium: European Committee for Standardization; 2004.
[27] Transport Scotland. Concrete half-joint deck structures. 2006.
[28] Loudon N. IAN 53/04 - Concrete half-joint deck structures 2004:18.
[29] Desnerck P, Lees JM, Valerio P, Loudon N, Morley CT. Inspection of RC half-joint bridges in England: analysis of current practice. Proc Inst Civ Eng - Bridg Eng 2018;171:290–302. https://doi.org/10.1680/jbren.18.00004.
[30] MIT CS dei L. Linee Guida per la classificazione e gestione del rischio, la valutazione della sicurezza ed il monitoraggio dei ponti esistenti. Tech Report. Cons Super Dei Lav Pubblici 2020.
[31] Di Carlo F, Meda A, Molaioni F, Rinaldi Z. Experimental evaluation of the corrosion influence on the structural response of Gerber half-joints. Eng Struct 2023;285:116052. https://doi.org/10.1016/j.engstruct.2023.116052.
[32] Granata MF, La Mendola L, Messina D, Recupero A. Assessment and strengthening of reinforced concrete bridges with half-joint deterioration. Struct Concr 2023;24:269–87. https://doi.org/10.1002/suco.202200367.
[33] Hamoudi AA, Phang MKS, Bierweiler RA. Diagonal shear in prestressed concrete dapped-beams. Acids J Proc 1975;vol. 72:347–50.
[34] Mattock AH, Chan TC. Design and behavior of dapped-end beams. PCI J 1979;24:28–45.
[35] Cardinale G, Orlando M. Structural evaluation and strengthening of a reinforced concrete bridge. J Bridg Eng 2004;9:35–42. https://doi.org/10.1061/(ASCE)1084-0702(2004)9:1(35).
[36] Mitchell D., Peng T., Cook W.D. Importance of Reinforcement Detailing. ACI Symp Publ n.d.;273. ⟨https://doi.org/10.14359/51682302⟩.
[37] Taher SE-DMF. Strengthening of critically designed girders with dapped ends. Proc Inst Civ Eng - Struct Build 2005;158:141–52. https://doi.org/10.1680/stbu.2005.158.2.141.
[38] Micheloni M, La Monica M, Parmeggiani D, Barchi P. Sustainable structural rehabilitation and strengthening of the "Ponte delle Grazie" bridge in Faenza, Italy. IOP Conf Ser Mater Sci Eng 2018;442:12021. https://doi.org/10.1088/1757-899X/442/1/012021.
[39] Zhou YE, Guzda MR. Bridge load rating through proof load testing for shear at dapped ends of prestressed concrete girders. Front Built Environ 2020;6.
[40] Palmisano F, Asso R, Chiaia B, Marano GC, Pellegrino C. Structural assessment of existing R.C. half-joint bridges according to the new Italian guidelines. J Civ Struct Heal Monit 2023;13:1551–75. https://doi.org/10.1007/s13349-022-00652-7.
[41] Spinella N, Messina D. Load-bearing capacity of Gerber saddles in existing bridge girders by different levels of numerical analysis. Struct Concr 2023;24:211–26. https://doi.org/10.1002/suco.202200279.
[42] Del Giudice G. Ponte a travata Gerber in cemento armato. Vital- e G Genova 1967.
[43] Schlaich J, Schäfer K, Jennewein M. Toward a consistent design of structural concrete. PCI J 1987;32:74–150.
[44] DIANA F.E.A.. DIANA Finite Element Analysis User's Manual Release 10.6. Delft, The Netherlands 2023.
[45] EN 12390–3. Testing hardened concrete - Part 3: Compressive strength of test specimens 2019.
[46] EN 12390–6. Testing hardened concrete - Part 6: Tensile splitting strength of test specimens 2010.
[47] EN 12390–13. Testing hardened concrete - Part 13: Determination of secant modulus of elasticity in compression 2021.
[48] UNI-EN-ISO. 6892–1. Metallic material tensile testing- Part 1: Method of test at room temperature 2020.